

# SnO<sub>2</sub>-Based Perovskite Solar Cells: Configuration Design and Performance Improvement

*Detao Liu, Yafei Wang, Hao Xu, Hualin Zheng, Ting Zhang, Peng Zhang, Feng Wang, Jiang Wu,\* Zhiming Wang, Zhi Chen, and Shibin Li\**

Organic-inorganic hybrid perovskite solar cells (PSCs) have developed rapidly in recent years owing to the low cost and high power conversion efficiency achieved. The excellent performance of PSCs is attributed to the superior electrical properties of each layer, including the electron transport layer (ETL), light-harvest layer, hole transport layer. As one of the most promising ETL materials for PSCs, SnO<sub>2</sub> shows excellent transmission, an appropriate energy band gap, a deep conduction band level, and high electron mobility, leading to efficient electron extraction and transport. Here, recent advancements in the PSCs with SnO<sub>2</sub> ETLs and endeavors aimed at improving the performance of this photovoltaic device are reviewed. Several typical configurations of SnO<sub>2</sub> based PSCs are discussed, including the planar structure, mesoporous structure, inverted structure and flexible PSCs. The efforts of modification and composite SnO<sub>2</sub> with other metal oxides are also assessed. Finally, an overview of the perspectives and challenges for the future of SnO<sub>2</sub> based PSCs is provided.

photovoltaic performance and low-cost fabrication process.<sup>[1–7]</sup> The brief development of PSCs has been listed in Figure 1a. Organic-inorganic hybrid perovskite materials (OIHP) are used as the light harvester layer. OIHP have the similar crystal structure as CaTiO<sub>3</sub> and the materials can be expressed as ABX<sub>3</sub> where A, B, and X are organic cation or I(A) group element, metal cation, and halide anion, respectively.<sup>[8–19]</sup> The A cation often stands for CH<sub>3</sub>NH<sub>3</sub><sup>+</sup>(MA<sup>+</sup>), HC(NH<sub>2</sub>)<sub>2</sub><sup>+</sup>(FA<sup>+</sup>), Cs, or Rb.<sup>[10–12,20–23]</sup> The B cation contains Sn<sup>2+</sup> or Pb<sup>2+</sup>.<sup>[24–30]</sup> The crystal structure of the OIHP is shown in the inset of Figure 1a. This family of materials exhibits numerous optical and electronic properties which is ideal for photovoltaic applications.<sup>[8,31,32]</sup> The OIHP have a large absorption coefficient and a tunable band gap.<sup>[21,25,33,34]</sup> The OIHP have a weak exciton binding energy, high-dual electron

and hole mobility, long carrier diffusion length, and high-defect tolerance, which is helpful for the dissociation of the photo-induced excitons into free carriers and helps the transport of the free carriers.<sup>[8,35]</sup>

## 1. Introduction

### 1.1. Unique Properties of Hybrid Perovskites

Perovskite solar cells (PSCs) are one of the third-generation solar cells and have been widely studied recently due to their perfect

Dr. D. Liu, Dr. Y. Wang, Dr. H. Zheng, Dr. T. Zhang, Dr. P. Zhang,  
Dr. F. Wang, Prof. Z. Chen, Prof. S. Li

State Key Laboratory of Electronic Thin Films and Integrated Devices,  
and School of Optoelectronic Science and Engineering  
University of Electronic Science and Technology of China (UESTC)  
Chengdu, Sichuan 610054, China  
E-mail: shibinli@uestc.edu.cn

Dr. H. Xu, Prof. J. Wu  
Department of Electronic and Electrical Engineering  
University College London  
Torrington Place, London WC1E 7JE, United Kingdom  
E-mail: jiang.wu@ucl.ac.uk

Prof. J. Wu, Prof. Z. Wang  
Institute of Fundamental and Frontier Sciences  
University of Electronic Science and Technology of China  
Chengdu, Sichuan 610054, China

Prof. Z. Chen  
Department of Electrical & Computer Engineering, and Center for  
Nanoscale Science & Engineering  
University of Kentucky  
Lexington, KY 40506, USA

DOI: 10.1002/solr.201800292

### 1.2. Brief History of Perovskite Solar Cells (PSCs)

OIHP was first introduced into solar cells as the light-harvesting layer reported by Kojima et al. in 2006.<sup>[36]</sup> They deposited CH<sub>3</sub>NH<sub>3</sub>PbBr<sub>3</sub> on mesoporous TiO<sub>2</sub> to replace the organic dye in dye sensitized solar cells (DSSCs) and obtained the solar cells with a power conversion efficiency (PCE) of 2.19%. In 2009, they replaced CH<sub>3</sub>NH<sub>3</sub>PbBr<sub>3</sub> with CH<sub>3</sub>NH<sub>3</sub>PbI<sub>3</sub> and increased the PCE to 3.81% due to the more suitable bandgap.<sup>[37]</sup> Subsequently, Park and his colleague employed similar structure in which perovskite sensitizer was deposited as quantum dots (QDs) in 2011. Compared with the dye sensitizer-N719, perovskite QDs showed a higher light absorption coefficient and the solar cells based on perovskite QDs obtained a PCE of 6.54%.<sup>[38]</sup> All above devices were based on the structure of DSSC whose sensitizer was soaked in liquid electrolyte. However, the perovskite materials can be dissolved into the electrolyte, so the performance of the solar cells degraded rapidly after it was prepared. To overcome this issue, in 2012, Kim et al.<sup>[39]</sup> utilized 2,2',7,7'-tetrakis(N,N-di-p-methoxyphenylamine)-9,9'-spirobifluorene (spiro-MeOTAD) to replace the

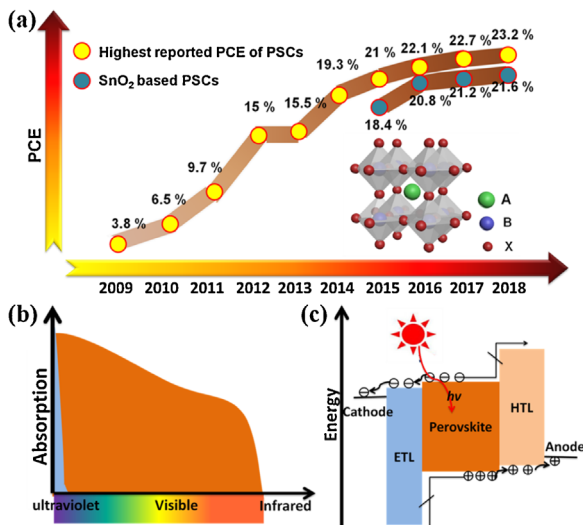
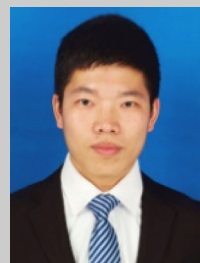


**Figure 1.** a) Brief development history of PSCs based on different ETLs (inset: crystal structure of perovskite materials), b) light absorption status in PSCs, and c) work mechanism of PSCs.

liquid electrolyte as the hole transport materials (HTM). The Spiro-MeOTAD is a solid material which can transport holes efficiently to the gold electrode. The introduction of solid HTM not only improved the stability of the solar cells, but also enhanced the PCE of the solar cells to 9.7%. In 2013, Burschka et al.<sup>[40]</sup> used sequential deposition methods to deposit perovskite layer to improve the morphology and obtained the solar cells with a PCE of 15%. In 2014, Zhou et al.<sup>[41]</sup> used polyethyleneimine ethoxylated to reduce the work function of the indium tin oxide (ITO). Combining the doping TiO<sub>2</sub> layer with Y element, they increased the PCE of PSCs to 19.3%. To tune the band gap to match the sunlight spectrum better, formamidinium (FA) was employed as the replacement or partial replacement of the methylamine (MA).<sup>[33,42–45]</sup> In 2015, Sang Il Seok's group utilized the intramolecular exchange method to deposit mixed-cation perovskite film, (FAPbI<sub>3</sub>)<sub>1-x</sub>(MAPbBr<sub>3</sub>)<sub>x</sub>, and gained perovskite with a perfect morphology.<sup>[22]</sup> The device based on the mixed-cation perovskite film yielded a PCE of 20.1%, which was the first report of the PCE more than 20%. In 2016, Gratzel's group introduced cesium element into the mixed-cation perovskite film to increase the temperature stability of the perovskite and obtained the device with a stabilized PCE of 21.1%.<sup>[11]</sup> To date, the highest PCE for PSCs is 23.2% reported.<sup>[46]</sup> The brief progress of the PSCs is shown in Figure 1a.

### 1.3. Electron Transport Layers of PSCs

PSCs consist of transparent conducting oxide (TCO), electrons transport layer (ETL), perovskite layer, holes transport layer (HTL), and metal contacts.<sup>[31,47–49]</sup> The perovskite layer absorbs most of visible light except some light absorbed by ETL (Figure 1b). The work mechanism of PSCs is shown in Figure 1c. Light is harvested by the perovskite layer and then electron-hole pairs are generated. The electron-hole pairs are separated by the built-in electric field. The electrons and holes mitigate toward ETL and HTL, respectively. Finally, electrons



**Detao Liu** is currently a Ph.D. candidate at the School of Optoelectronic Science and Engineering, University of Electronic Science and Technology of China. He received his B.S. Degree in Electronics Science and Technology from University of Electronic Science and Technology of China in 2014. His research interests focus on the compositional engineering of perovskite materials.



**Jiang Wu** received a B.S. degree from the University of Electronic Science and Technology of China (UESTC), Chengdu, China, and M. Sc. and Ph.D. degrees in electrical engineering from the University of Arkansas, AR, USA, in 2008 and 2011, respectively. After his Ph.D., he joined the State Key Laboratory of Electronic Thin Films and Integrated Devices at UESTC. Since 2012, he has been with the Photonics Group as a Research Associate working on Molecular Beam Epitaxy of III–V compound semiconductors and optoelectronic devices. He is currently a Lecturer in the Department of Electronic and Electrical Engineering, University College London, London, U.K.



**Shibin Li** is currently a Professor in the School of Optoelectronic Science and Engineering at the University of Electronic Science and Technology of China (UESTC). He received his Ph.D. from UESTC in 2008. He joined the Department of Electrical & Computer Engineering at the University of Kentucky and University of Arkansas, USA, as a postdoctoral fellow in 2008 and 2009, respectively. He was an associate professor with UESTC from 2011 before his current position. His research group focuses on nanoscale materials for solar cells, flexible sensors, and photodetectors.

and holes accumulate at cathode and anode, respectively. When a wire connection between cathode and anode is added, current appeared due to the diffusion of charges. The electron transport materials often belong to N-type semiconductor class. It is used to extract electrons from light-harvest layer and block holes to recombine with electrons in cathode. So the materials used as ETL must satisfy following qualifications: a) a high electron mobility; b) a good energy level matching with the perovskite films; and c) having an easy way to fabricate high-quality films.

In the normal structure, the materials are required to have a wide bandgap and a good transmittance in the visible light range, assisting the reduction of light energy loss. Some metal oxides and organic materials have been developed as the ETL.<sup>[50–62]</sup>

TiO<sub>2</sub> is the most widely used materials as the ETL for PSCs. It has a bandgap of 3.6 eV and the wide bandgap guarantees the transmittance of the most light in the visible range.<sup>[63]</sup> Additionally, the energy level matches with the perovskite band structure well, and the PSCs with the highest PCE record are based on this material.<sup>[64–66]</sup> However, the electron mobility is only in the range of  $0.14 \text{ cm}^2 \text{ V}^{-1} \text{ s}^{-1}$ , which is lower than the electron mobility of perovskite.<sup>[63]</sup> Low-mobility materials cannot transport the electron extracted from perovskite to electrodes timely and resulting in the accumulation of charges near the interface, which could affect the further charge extraction from perovskite film. So introducing nanostructures like the mesoporous TiO<sub>2</sub> layers in TiO<sub>2</sub>-based PSCs can increase the contact area at the interface between perovskite and electron transport layer, resulting in a diluted charge concentration near the interface and a more sufficient further charge extraction from perovskite.<sup>[67,68]</sup> Thus, mesoporous TiO<sub>2</sub>-based PSCs yield a better photovoltaic performance compared with planar TiO<sub>2</sub> based PSCs. TiO<sub>2</sub> films also need be annealed at a high temperature to confirm the proper crystalline, resulting in higher cost and limitation of further applications.<sup>[40,51,69–74]</sup> ZnO is also a material used as ETL widely. It has a higher electron mobility and deeper conduction band level compared with TiO<sub>2</sub>.<sup>[75]</sup> Additionally, a ZnO film can be prepared at a much lower temperature, which is compatible with the fabrication process of flexible PSCs.<sup>[76–78]</sup> The highest PCE of PSCs based on ZnO is about 21% which is very close to the best efficiency of PSCs.<sup>[79]</sup> However, a perovskite film is decomposed easily on a pristine ZnO film under illumination or high-temperature condition.<sup>[79–82]</sup> Besides the above metal oxides, other metal oxides such as NbO<sub>x</sub>, WO<sub>x</sub>, BaSnO<sub>3</sub>, and CeO<sub>x</sub>, also have been employed as ETL materials, but these materials have not caught a lot of attention.<sup>[61,83–88]</sup> Fullerene and its derivatives also have been developed as the ETL widely.<sup>[54,57,60,89–95]</sup> These materials are often used as the ETL in the inverted structure due to their solubility in organic solvent and low-light transmittance. Although these materials have low-electron mobility, they can passivate the defect of the perovskite surface efficiently and high-performance PSCs can also be obtained through optimizing the ETL. However, these organic materials are much more expensive than inorganic materials and they are not compatible with the commercialization of PSCs. The price for fullerene and its derivatives is at least 411 dollar/g according to the Sigma-Aldrich website, which is much higher than the prices of the precursors for TiO<sub>2</sub> and SnO<sub>2</sub> (titanium diisopropoxide bis(acetylacetone): 36.30 dollars/(100 mL), SnCl<sub>4</sub>: 45.5 dollars/(5 g)).

SnO<sub>2</sub> is a promising alternative to TiO<sub>2</sub> due to its perfect optical and electronic properties. First of all, SnO<sub>2</sub> has a much higher electron mobility ( $421.70 \text{ cm}^2 / (\text{V} \cdot \text{s})$ ) than TiO<sub>2</sub>, and it can ensure the efficient transport of electrons, thus, most of PSCs based on SnO<sub>2</sub> do not need nanostructures.<sup>[96–98]</sup> Secondly, SnO<sub>2</sub> also has a wider energy bandgap compared with TiO<sub>2</sub>, resulting

in better transmittance and less light energy loss in PSCs.<sup>[50]</sup> The wider bandgap also makes the ETL more stable under UV illumination.<sup>[99]</sup> Thirdly, ITO and fluorine-doped tin oxide (FTO) consist of SnO<sub>x</sub>. It means that there is smaller refractive index gradient between the TCO and SnO<sub>2</sub> compared with TiO<sub>2</sub>, which can reduce the reflection of light. Last but not the least, the annealing temperature for SnO<sub>2</sub> film is lower than 180 °C, signifying that solar cells can be fabricated with a lower cost and thermal budget.<sup>[51,100,101]</sup> The lower-temperature annealing also makes it compatible with the fabrication process of flexible PSCs. Until now, the highest PCE for PSCs based on SnO<sub>2</sub> has reached more than 21%, which is the highest PCE for the planar structure PSCs.<sup>[102–104]</sup> The development of SnO<sub>2</sub>-based PSCs is shown in Figure 1a.

In this review, we briefly summarize the different methods to fabricate the SnO<sub>2</sub> ETL for PSCs. The main text includes two parts. The first part has introduced the different structures of the PSCs based on SnO<sub>2</sub> including normal structure, inverted structure, and flexible substrate-based structure. The second part summarizes the various methods to improve the electrical properties of SnO<sub>2</sub>. These methods include doping SnO<sub>2</sub> with other elements and interface modification. The second part also introduces combining SnO<sub>2</sub> with other metal oxides as the ETL of PSCs. Different metal oxides acting different roles in PSCs are reviewed. Each part has introduced different methods to deposit SnO<sub>2</sub> films and explained the performance improvement mechanism of PSCs. This review tends to present a timely update on the recent development of SnO<sub>2</sub> ETL-based PSCs and provides some guidelines for further optimization and design of PSCs based on SnO<sub>2</sub> ETLs and beyond.

## 2. Configurations of SnO<sub>2</sub>-Based PSCs

It is well-known that PSCs originated from DSSCs, so the initial structure of PSCs is similar to DSSCs, which is called normal structure. The conventional structure of DSSC contains mesoporous TiO<sub>2</sub> layer. As a result, the initial normal structure of PSCs also contained mesoporous metal oxide layer and the mesoporous structures included nanorods, nanotubes, and nanowires.<sup>[37,69,105–108]</sup> In 2012, Snaith's group demonstrated that perovskites were able to transport both electrons and holes, which was different from the organic dye sensitizer of DSSC.<sup>[109]</sup> Since then, the PSCs without nanostructure in perovskite film, called planar PSCs, appeared. Inspired by the structure of the organic solar cells, PSCs with an inverted structure has been developed. The structure schematic diagram of PSCs based on different structures are shown in Figure 2a–c. The SnO<sub>2</sub> materials has various structures such as nanoparticles, nanowires, and nanotubes obtained from different fabrication methods. Therefore, the structures of normal PSCs based on SnO<sub>2</sub> also include planar structure and mesoporous structure. The SnO<sub>2</sub> films can be fabricated through low-temperature methods and it is compatible with the fabrication process of flexible PSCs. We divide this section into four parts according to the structure of PSCs, and various SnO<sub>2</sub> film deposition methods which are suitable for different structures have been summarized in each part.

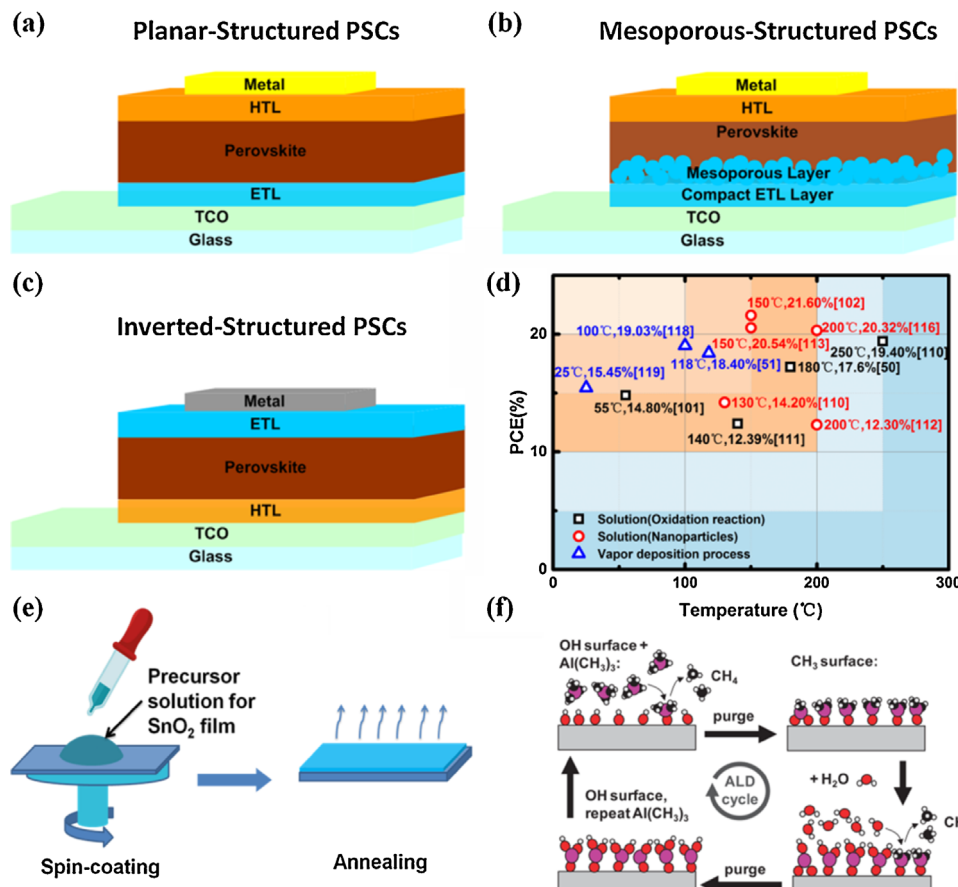


**Figure 2.** a–c) Diagrams of perovskite solar cells based on different structures. d) PCE statistics of planar PSCs with different process temperature and deposition methods. e) Deposition process of  $\text{SnO}_2$  based on spin-coating. f) diagram of atomic layer deposition process. Reproduced with permission.<sup>[117]</sup> Copyright 2011, Materials Research Society.

## 2.1. Planar Structure PSCs

To date, the vast majority of PSCs based on  $\text{SnO}_2$  are the planar structure PSCs due to their efficient collection of electrons. There are two mainstream methods to prepare  $\text{SnO}_2$  ETL for planar PSCs. The first method is based on solution process, and the other one is based on vapor deposition process. Solution methods include spin-coating and chemical bath deposition (CBD) method. One of the important aims of developing different deposition methods is to decrease the deposition temperature and reduce the thermal budget. Figure 2d shows the various results of planar  $\text{SnO}_2$ -based PSCs with different deposit methods and process temperature.

Fang's group introduced  $\text{SnO}_2$  as the ETL of PSCs first time in 2015.<sup>[50]</sup> The  $\text{SnO}_2$  film was prepared through spin-coating  $\text{SnCl}_2 \cdot 2\text{H}_2\text{O}$  precursor of which solvent was ethanol, and then thermally annealed in the air at 180 °C for 1 h, as shown in Figure 2e. The  $\text{SnCl}_2 \cdot 2\text{H}_2\text{O}$  precursor was oxidized into  $\text{SnO}_2$  at a high temperature by oxygen. Compared with compact  $\text{TiO}_2$ -coated FTO glass, the  $\text{SnO}_2$ -coated FTO glass has much better light transmittance due to its anti-reflection and wider band gap. According to the XPS analysis of the film, the precursor was transformed into  $\text{SnO}_2$  completely. After optimizing the

thickness of  $\text{SnO}_2$ , it has been achieved that the best-performing planar PSCs based on  $\text{MAPbI}_3$  using a  $\text{SnO}_2$  ETL possessed PCE of 17.21% when measured under reverse voltage scanning direction, respectively. They further explored the effects of annealing temperature of  $\text{SnO}_2$  on the performance of PSCs.<sup>[97]</sup> It was shown that the film with an annealing temperature of 500 °C appeared agglomerate seriously thus left many uncovered FTO areas, which could not effectively block holes and might lead to severe interface recombination. It was also clarified that the band gap of the high-temperature annealed  $\text{SnO}_2$  (HT- $\text{SnO}_2$ ) was slightly narrower than the low-temperature annealed  $\text{SnO}_2$  (LT- $\text{SnO}_2$ ) and the conduction band edge of HT- $\text{SnO}_2$  was further from the conduction band edge of perovskite. High-temperature annealing also led to dramatic increase of the free-electron density. These electrons might recombine with holes and led to a weaker ability to block holes, so that PSCs based on LT- $\text{SnO}_2$  had a much better performance compared with PSCs based on HT- $\text{SnO}_2$ . The mechanism of the enhanced conductivity and increased free-electron density was explored by Roose et al.<sup>[99]</sup> They found that the fluorine migration from FTO to ETL caused  $\text{SnO}_2$  electronically equivalent to FTO when  $\text{SnO}_2$  film was treated at high temperature. Jung et al. adopted tin (IV) isopropoxide as the precursor to deposit  $\text{SnO}_2$ .<sup>[110]</sup> They

dissolved tin (IV) isopropoxide into isopropanol and spin-coated it on FTO glass in a glove box filled with N<sub>2</sub>. Then the substrates were dried at 65 °C on hotplate for 1 min and heated further in the furnace in ambient condition at different temperature after pre-drying. The mixed cation perovskite (FAPbI<sub>3</sub>)<sub>0.875</sub>(CsPbI<sub>3</sub>)<sub>0.125</sub> was deposited as the light harvester. It was found that different annealing temperature of SnO<sub>2</sub> could affect the performance and hysteresis of PSCs, and the annealing temperature of 250 °C had obtained the best-performing PSCs with a PCE of 19.4%.

In 2016, Liu et al. used a dual-fuel combustion method to prepare SnO<sub>2</sub>. The precursor solution is prepared by the following steps.<sup>[111]</sup> First, SnCl<sub>2</sub> and NH<sub>4</sub>NO<sub>3</sub> were dissolved in 2-methoxyethanol and stirred at room temperature for 1 h. Then, urea was added into the solution and stirred at room temperature for another 1 h. After aging for 48 h, acetylacetone was added into the solution and stirred for another 1 h, followed by aging for another 18–24 h. The SnO<sub>2</sub> film was deposited by spin-coating, and then annealed at 140 °C for 1.5 h. After optimizing the process and quantity of additive, the highest PCE of the PSCs based on the pristine SnO<sub>2</sub> deposited by this method reached 12.39%. Although this method did not obtain high-performing PSCs, it had lowered the preparation temperature of SnO<sub>2</sub> to 140 °C.

Furthermore, Barbe et al. used the CBD method to prepare amorphous SnO<sub>2</sub>, which lowered the deposition temperature to 55 °C.<sup>[101]</sup> The amorphous film was formed on the substrate by placing substrate face down in the aqueous solution of SnCl<sub>4</sub> · H<sub>2</sub>O at 55 °C with stirring at 400 rpm (round per minute) for 11.5 min. The process did not require spin-coating and post-annealing treatment. PSCs based on this amorphous film had gain a PCE of 14.8%. This method was not only simple but also compatible with large-scale manufacture process of PSCs.

Another solution-based deposition is using the pre-crystallized SnO<sub>2</sub> nanoparticles as the precursor. Tian and his co-workers dispersed the SnO<sub>2</sub> nanoparticles (ca. 22–43 nm) in butanol as the precursor solution in 2015.<sup>[112]</sup> They spin-coated the solution on substrates and baked it at 200 °C for 1 h. Perovskite film was deposited by a two-step sequential deposition method. In the preparation process of the perovskite film, PbI<sub>2</sub> film was treated with solvent vapor annealing (SVA). It was found that the PbI<sub>2</sub> crystal size increased and the cavity number on the surface of PbI<sub>2</sub> also increased. The increased cavity number assisted the penetration of methylammonium iodide (MAI) and promoted the reaction of the precursors during a certain period of time. The SnO<sub>2</sub>-based PSCs with a PCE of 12.3% had been obtained ultimately. Compared with TiO<sub>2</sub>-based PSCs, the performance of SnO<sub>2</sub>-based PSCs was much more stable. In most of SnO<sub>2</sub>-based PSCs, the thickness of ETL is in the range of 20–100 nm, so the large-scale SnO<sub>2</sub> nanoparticles as the precursor of ETL would induce a lot of pinholes, which led to direct contact between cathode and perovskite and caused severe recombination. Jiang et al. used smaller-scale SnO<sub>2</sub> nanoparticles (ca. 3–4 nm) which was dispersed in water as the precursor of ETL.<sup>[113]</sup> They spin-coated solution on glass/ITO substrates at 3000 rpm for 30 s and then annealed it on a hot plate in ambient air at 150 °C for 30 min. This method obtained a dense, pinhole-free SnO<sub>2</sub> film due to the much smaller size of nanoparticles. The film showed good transparency with transmission values greater than 95% in the visible region, and it minimized optical loss in the ETL. The light harvester of PSCs was

(FAPbI<sub>3</sub>)<sub>x</sub>(MAPbBr<sub>3</sub>)<sub>1-x</sub>. Some MACl was added into the precursor solution and the film was annealed in ambient air after second-step spin coating, which contributed to the high-quality perovskite film. After high temperature annealing, some excess PbI<sub>2</sub> was formed and the planar PSCs with excess PbI<sub>2</sub> had better performance. The best device performances of planar PSCs using SnO<sub>2</sub> nanoparticles as the ETL yielded a PCE of 20.54% under forward scan direction and there was negligible hysteresis. Furthermore, Jiang et al. systematically investigated the effect of precise stoichiometry like the PbI<sub>2</sub> content.<sup>[102]</sup> They found that a moderate residual of PbI<sub>2</sub> could contribute to the stable and high efficiency of planar PSCs without hysteresis. Ultimately, they gained the planar structure PSCs with efficiency beyond 21% which is very closed to the highest reported PCE for planar structure PSCs to date. Above nanoparticles were synthesized by others and those articles did not refer to the methods to prepare nanoparticles. Abulikemu et al. used a microwave-assisted non-aqueous sol-gel route to synthesize the SnO<sub>2</sub> nanoparticles.<sup>[114]</sup> This method was similar to the synthesis route by Ba et al. except the heating way.<sup>[115]</sup> In the synthesis process, 0.85 mL SnCl<sub>4</sub>, 3 mL ethanol, and 17 mL benzyl alcohol were added and mixed in a 20 mL microwave vial inside a glovebox. After sealing with a cap, the vial was transferred to a microwave reactor cavity and the reaction temperature was set to 130 °C for two different times (1.5 h and 5 h). After the reaction was completed, the final product was washed for three times and dispersed into ethanol. From the transmission electron microscopy of nanoparticles, the average size of nanoparticles grown for 1.5 h and 5 h was approximately 3 nm and 10 nm, respectively. The nanoparticle dispersion was spin-coated on ITO/glass substrates and then the substrates were used to fabricate complete PSCs based on CH<sub>3</sub>NH<sub>3</sub>PbI<sub>3</sub>. The best performing solar cells with 3 nm SnO<sub>2</sub> nanoparticles ETL had a PCE of 14.2%. Yang et al. also reported that using colloidal SnO<sub>2</sub> nanoparticles as the ETL materials of PSCs.<sup>[116]</sup> They introduced thiourea into the SnCl<sub>2</sub> · H<sub>2</sub>O solution to accelerate and stabilize the formation of the SnO<sub>2</sub> QDs (Figure 2d). After the formation of the SnO<sub>2</sub> QDs, the solution was spin-coated onto the FTO substrates treated with different temperature, ranging from 50 to 250 °C. When the SnO<sub>2</sub> films were heated at higher temperature, S-group vaporized more quickly and more oxygen vacancies were formed, resulting in a higher electron density/conductivity. The study controlled the annealing temperature to adjust the carrier concentration and optimized the photovoltaic performance. The PSCs showed the best performance with SnO<sub>2</sub> QDs ETLs annealed at 200 °C. The champion PSCs based on Cs<sub>0.05</sub>(MA<sub>0.17</sub>FA<sub>0.83</sub>)<sub>0.95</sub>Pb(I<sub>0.83</sub>Br<sub>0.17</sub>)<sub>3</sub> (CsMAFA) achieved an excellent stabilized power output of 20.32%.

The deposition methods based on solution process is low-cost and simple, but most of them include the spin-coating process, which is not compatible with the large-scale manufacture of solar cells. Therefore, some deposition methods based on vapor deposition has been employed to deposit the SnO<sub>2</sub> film as ETL. The deposition temperature can also be lowered apparently. The vapor deposition methods include chemical vapor deposition and physical vapor deposition.

Chemical vapor atomic layer deposition (ALD) process is one of the most promising methods to deposit the highly compact and ultra-thin metal oxide and its deposition process diagram is shown in Figure 2f (taking the deposition of Al<sub>2</sub>O<sub>3</sub> as the example).<sup>[117]</sup> In

2015, Hagfeldt's group used ALD process to prepare  $\text{SnO}_2$  film as the ETL of planar PSCs.<sup>[51]</sup> To make this process compatible with upscaling process and tandem devices, ozone, showing much stronger oxidizability than water, was used as the oxygen precursor, and tetrakis (dimethylamino) tin (IV) (TDMA-Sn) was used as the tin precursor. It had lowered the deposition temperature to 118 °C.  $\text{TiO}_2$  was also deposited using ALD at low temperature as the reference. According to ultraviolet photoelectron spectroscopy (UPS) and femtosecond transient absorption (TA) measurements, it was found that pristine  $\text{SnO}_2$  ETL had better electron extraction than  $\text{TiO}_2$  ETL because of the favorable energetic alignment. Mixed perovskite ( $(\text{FAPbI}_3)_{0.85}(\text{MAPbBr}_3)_{0.15}$ ) film was spin-coated as the light harvester layer and planar structure PSCs with a PCE of 18.4% were fabricated. Compared with planar PSCs based on  $\text{TiO}_2$ , the planar PSCs based on  $\text{SnO}_2$  had a negligible hysteresis behavior. Besides the ozone, oxygen plasma also has strong oxidizability and can reduce the deposition temperature as well. So in 2016, Wang et al. used plasma-enhanced ALD to deposit  $\text{SnO}_2$  film and lower the deposition temperature below 100 °C.<sup>[118]</sup> They also used TDMA-Sn as the Sn precursor and pure  $\text{O}_2$  as the oxidizer. When the  $\text{O}_2$  was injected into the chamber, the  $\text{O}_2$  plasma was generated by a plasma generator. The resulting deposition rate was about 0.17 nm per cycle.  $\text{SnO}_2$  films with different deposition cycles were employed as the ETLs for planar PSCs. The photovoltaic performance of planar PSCs showed that  $\text{SnO}_2$  film deposited with 130 cycles as the ETL showed the best performance.

In 2017, Chen et al. adopted pulse laser deposition (PLD) to deposit  $\text{SnO}_2$  film. The  $\text{SnO}_2$  was evaporated by a KrF laser (248 nm) which was focused onto the  $\text{SnO}_2$  rotating target, and the vapor gathered at FTO/ITO substrate to form the complete film.<sup>[119]</sup> These processes were carried out under 15 Pa of oxygen background pressure. The thickness of ETL had a great influence

on the performance of PSCs, so they fixed the deposition oxygen partial pressure and changed the deposition time to optimize the thickness of  $\text{SnO}_2$  film. Compared with PSCs with the thinner ETL samples (4 nm or 6 nm), the PSCs with  $\text{SnO}_2$  films with a thickness of 8 nm showed better performance due to the higher shunt resistance. When the film thickness was increased to 10 nm, the short-circuit current density ( $J_{\text{SC}}$ ) began to decrease and the PCE also began to decrease due to the higher series resistance ( $R_S$ ). To identify the effect of deposition temperature on the performance of PSCs, the  $\text{SnO}_2$  films deposited with different temperature were prepared as the ETL. It was found that the higher temperature did not bring improvement in the performance but more cost of fabrication compared with room temperature. Thus, using PLD to deposit  $\text{SnO}_2$  did not need any annealing process during or after the deposition, and PSCs based on  $\text{MAPbI}_3$  gained a PCE of 15.45%. This method decreased the deposition temperature of  $\text{SnO}_2$  as the ETL of PSCs to room temperature, which is important for fabrication of flexible solar cells.

According to above discussion about  $\text{SnO}_2$  fabrication methods, it can be concluded that the annealing temperature of  $\text{SnO}_2$  film influences photovoltaic performance of PSCs dramatically. It is well-known that a higher-temperature annealing increases the crystallinity of metal oxide. So it is very meaningful to discuss the role of the crystallinity of  $\text{SnO}_2$  on photovoltaic performance of PSCs intensively here. The  $\text{SnO}_2$  films obtained from low-temperature chemical reactions including vapor deposition process and solution-based oxidation process directly show amorphous initially.<sup>[120–122]</sup>  $\text{SnO}_2$  films are crystallized and show a tetragonal rutile crystallization after annealed at a temperature more than 400 °C.<sup>[120,122]</sup> From Figure 3d, the temperature lower than 200 °C is favorable for

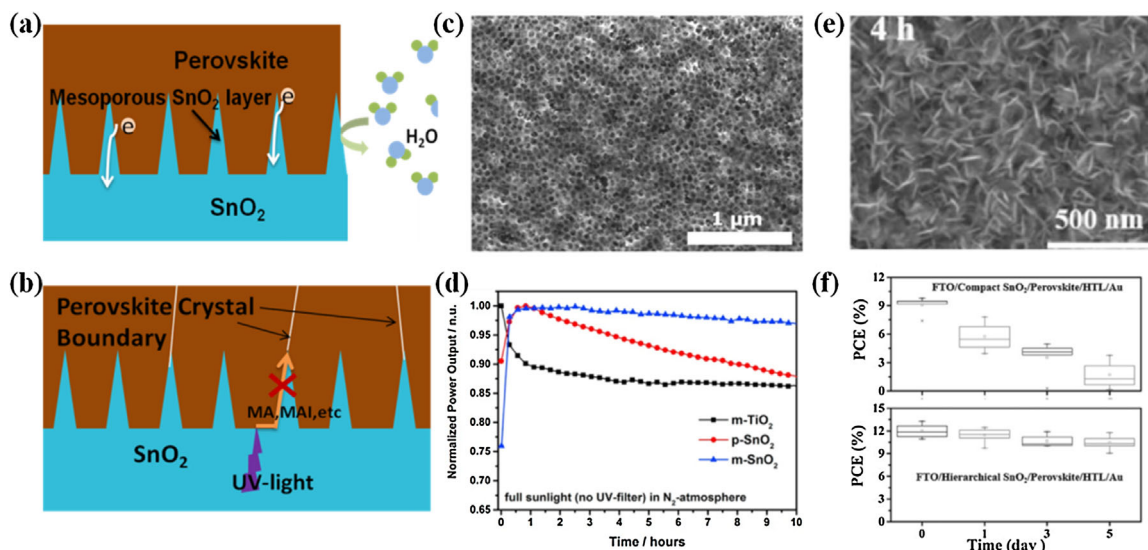


**Figure 3.** a) Schematic diagram for how mesoporous layer promotes electron transfer and improves moisture stability. b) schematic diagram for how mesoporous layer improves UV-light stability. c) SEM image of a mesoporous  $\text{SnO}_2$  film synthesized by block-copolymer assisted self-assembly. d) maximum power output variation for mesoporous  $\text{SnO}_2$ , mesoporous  $\text{TiO}_2$  and planar  $\text{SnO}_2$  employing PSCs with exposure time under AM1.5 simulated solar light (100  $\text{mW cm}^{-2}$ ) illumination. Reproduced with permission.<sup>[99]</sup> Copyright 2016, Elsevier. e) Top view SEM images of the  $\text{SnO}_2$  morphology after hydrothermal reaction for 4 h. f) box chart data of PCEs for 10 PSCs without and with hierarchical  $\text{SnO}_2$  ETL (stored in  $\approx 70\%$  humidity). Reproduced with permission.<sup>[126]</sup> Copyright 2016, Wiley-VCH.

high-performance PSCs. However, the high-temperature annealing process not only increases the crystallinity but also changes the morphology of  $\text{SnO}_2$  films. The high-temperature annealing process crystallizes  $\text{SnO}_2$  film after the amorphous  $\text{SnO}_2$  film has been obtained, resulting in serious agglomeration of  $\text{SnO}_2$  and appearance of uncovered electrode. The incomplete coverage of  $\text{SnO}_2$  induces serious charge recombination and deteriorate the performance of PSCs.<sup>[97,122]</sup> Hence, it does not mean a  $\text{SnO}_2$  film with a tetragonal rutile crystallization is unfavorable for high-performance PSCs. It is also vital to identify how the high-temperature annealing affects the photovoltaic performance. The nanoparticles or nanocrystals used to prepare  $\text{SnO}_2$  film often show high crystallinity.<sup>[102,113,116,123]</sup> Hence, the films deposited from spin-coating nanoparticles or nanocrystals often have a tetragonal rutile crystallization. Most of PSCs based on these films show an excellent photovoltaic performance and the highest PCE of PSCs based on highly-crystallized  $\text{SnO}_2$  reaches 21.60% which is much higher than that of PSCs based on amorphous  $\text{SnO}_2$  film.<sup>[102,113,116,123]</sup> From the above discussions in this paragraph, the highly crystallized  $\text{SnO}_2$  with full coverage is favorable for high-performance PSCs, and the performance deterioration of PSCs results from the incomplete coverage of crystallized  $\text{SnO}_2$  after high-temperature annealing amorphous  $\text{SnO}_2$ .

## 2.2. Mesoporous Structure PSCs

Although the planar  $\text{SnO}_2$  PSCs have achieved a high performance, they also suffered from the serious instability. The water molecules can invade the perovskite film from the side face and decompose the film easily. Although  $\text{SnO}_2$  has wide band gap and shows few photocatalysis, the UV-light can penetrate the ETL and decompose the perovskite directly. As shown in Figure 3a, introducing a mesoporous layer not only enhances the electron collection efficiency through shortening the electron transport length in perovskite, but also retards the moisture penetration from the side face, which improves the long-term stability of the PSCs. The mesoporous layer has more surface to contact with perovskite. Therefore, the mesoporous layer can improve the adhesion of perovskite film. The mesoporous structure can also act a cage to limit the migration of by-products generated by decomposition of perovskite (Figure 3b), which further enhance UV stability of PSCs.

The first report about mesoporous structure PSCs based on  $\text{SnO}_2$  was in 2015. Dong et al. dissolved  $\text{SnCl}_2 \cdot 2\text{H}_2\text{O}$  in ethyl alcohol as the  $\text{SnO}_2$  organic sol.<sup>[124]</sup> Before using the solution, it was stirred for 3 h at 80 °C, then aged for 3 h at 30 °C and 24 h at room temperature. The compact  $\text{SnO}_2$  ETL was prepared through spin-coating  $\text{SnO}_2$  organic sol on FTO glasses and then sintered them in a furnace at 450 °C for 2 h. After exploring different concentration of the organic sol as the precursor of  $\text{SnO}_2$  ETL, they found that 0.5 M was the optimum concentration. Compared with the  $\text{TiO}_2$  as the ETL,  $\text{SnO}_2$  used as ETL needed a larger thickness to cover the FTO completely due to the larger size of  $\text{SnO}_2$  nanoparticles. The  $\text{SnO}_2$  samples were identified as the tetragonal rutile phase according to X-ray diffraction (XRD). After depositing  $\text{SnO}_2$ , a layer of mesoporous  $\text{TiO}_2$  was spin-coated on the compact layer and then

sintered at 500 °C. The perovskite layer was deposited by two step method and HTL was spin-coated on the perovskite. Finally, a layer of Ag was thermally evaporated on the HTL. The current–voltage ( $J$ – $V$ ) curves of the devices based on different ETLs exhibited that the PSCs based on  $\text{SnO}_2$  (S-PSCs) had larger  $J_{SC}$  but lower  $V_{OC}$  and fill factor (FF) compared with PSCs based on  $\text{TiO}_2$  (T-PSCs). The higher  $J_{SC}$  meant that the  $\text{SnO}_2$  had higher conductivity. The more positive shift of the  $\text{SnO}_2$  conductive band caused the faster interfacial recombination at the interface between the  $\text{SnO}_2$  and perovskite.

Zhu et al. used a simple silica-templated hydrothermal method to synthesize mesoporous  $\text{SnO}_2$  single crystals (MSCs).<sup>[125]</sup> The SEM and TEM images of the mesoporous  $\text{SnO}_2$  single crystals indicated that the average width was 150–200 nm and length was 500–1  $\mu\text{m}$ . The mesoporous  $\text{SnO}_2$  single crystals ( $\text{SnO}_2$  MSC) were spin-coated on FTO as the electron collecting layer for PSCs without the compact layer, and the perovskite layer was deposited by a two-step method. However, the device had a relatively low PCE of 3.76% due to the strong recombination. After depositing the mesoporous layer, the substrate was treated with  $\text{TiCl}_4$  aqueous solution at 70 °C for 0.5 h and heated at 500 °C for 0.5 h, and a thin  $\text{TiO}_2$  film was formed on the mesoporous layer by this treatment, which improveded the PCE to 8.54%.

Roose et al. introduced the mesoporous  $\text{SnO}_2$  layer to enhance the stability of PSCs under continuous full sunlight illumination in an inert atmosphere.<sup>[99]</sup> They used aluminum-doped zinc oxide as the transparent conductive oxide electrode to inhibit fluorine migration of FTO substrates when heated at high temperature. After depositing the compact  $\text{SnO}_2$  film, a layer of mesoporous  $\text{SnO}_2$  was fabricated on the substrate. The mesoporous  $\text{SnO}_2$  was synthesized via block-copolymer assisted self-assembly. Poly (1,4-isoprene-b-ethylene oxide) (25 mg, Polymer Source, Mn:PIp(50000)-PEO(12000), Mw/Mn: 1.05) was dissolved in tetrahydrofuran (1 mL) to prepare a tin oxide precursor sol and the resulting solution was spin-coated onto the substrate. The film was annealed on a programmable hotplate to remove the block-copolymer template and recrystallize  $\text{SnO}_2$ . The mesoporous  $\text{SnO}_2$  layer was formed finally. XRD pattern of the mesoporous layer showed the formation of rutile  $\text{SnO}_2$ . Triple citation perovskite was used as the light absorber layer and Spiro-OMeTAD as the hole transport layer. PSCs based on mesoporous  $\text{SnO}_2$  with a PCE of 13.1% has been obtained. Then the maximum power output for PSCs based on mesoporous  $\text{TiO}_2$ (m- $\text{TiO}_2$ ), mesoporous  $\text{SnO}_2$ (m- $\text{SnO}_2$ ) and compact  $\text{SnO}_2$  (c- $\text{SnO}_2$ ) exposed to AM1.5 simulated solar light (100 mW cm<sup>-2</sup>) illumination for a long time was measured. UV-stability of the PSCs manifest that the PSCs with mesoporous  $\text{SnO}_2$  layer had the best stability among these PSCs, as shown in Figure 3d.

Besides above spin-coating method to deposit mesoporous  $\text{SnO}_2$  layer, the hydrothermal method, commonly used to grow nanostructures and microstructures, was developed to grow mesoporous  $\text{SnO}_2$  layer onto substrate directly.<sup>[126–130]</sup> Liu et al. used low-temperature hydrothermally grown hierarchical nano- $\text{SnO}_2$  as the electron transport layers.<sup>[126]</sup> The precursor solution was prepared by the following steps. Hexamethylenetetramine and tin oxalate power were added into a white mouth bottle. Then deionized water was added into the bottle to dissolve the solute and the solution with a concentration of 0.025 M was

obtained. Subsequently, the mixture was stirred under ambient conditions for 1 h. The FTO substrates were dipped into the precursor solution and the hydrothermal growth was conducted inside a laboratory oven which was kept at 95 °C for 0–10 h. The SEM images showed that there were some SnO<sub>2</sub> nanoparticles grown on the surface of the substrate at the beginning of the reaction. After 2 h, the FTO substrate was covered by the SnO<sub>2</sub> nanoparticles completely and a compact SnO<sub>2</sub> film was formed. Some discontinuous nanosheets emerged on the compact layer with the increasing hydrothermal reaction time. With the longer reaction time, more larger and thicker SnO<sub>2</sub> nanosheets were grown and a continuous SnO<sub>2</sub> nanosheet network was gained eventually. The top view SEM images of the SnO<sub>2</sub> morphology after hydrothermal reaction for 4 h is shown in Figure 3e. The full survey XPS spectrum and the XRD pattern of the film indicated that the composition of the final film prepared by the hydrothermal method was pure SnO<sub>2</sub>. PSCs with various growth time of the ETL on the substrate were fabricated to identify the photovoltaic performance. The *J*–*V* curves and incident photon-to-current conversion efficiency (IPCE) of PSCs based on SnO<sub>2</sub> with different growing time suggested that the SnO<sub>2</sub> film grown for 4 h was appropriate for the optimum performance of PSCs. The performance of champion PSC with the optimum SnO<sub>2</sub> film had a PCE of 16.17%, a *J*<sub>SC</sub> of 22.76 mA cm<sup>-2</sup>, a FF of 68.0%, and a *V*<sub>OC</sub> of 1.05 V. A comparative study of 5 days' stability measurement for the PSCs with mesoporous SnO<sub>2</sub> ETLs versus compact SnO<sub>2</sub> ETLs and without ETL under 70% humidity was performed. The results shown in Figure 3f demonstrated that PSCs using mesoporous SnO<sub>2</sub> layer made PSCs have a better moisture-stability compared with planar PSCs and also show excellent long-term stability.

### 2.3. Inverted Structure PSCs

The inverted structure of PSCs originated from the structure of the organic solar cells. The P/N type organic semiconductor was used as the holes/electrons selecting layer at first.<sup>[57,68,90,131–133]</sup> However, ETLs fabricated from organic semiconductor materials are not as compact as those fabricated from inorganic semiconductor materials. Organic semiconductor materials have a much higher cost compared with inorganic semiconductor materials as well. So a lot of inorganic semiconductors were introduced to PSCs based on inverted structure.<sup>[52,123,134–139]</sup> The ideal inorganic N-type semiconductor materials includes TiO<sub>2</sub>, SnO<sub>2</sub>, ZnO, etc.<sup>[52,123,134–136]</sup> Nevertheless, the above inorganic materials as the electron transport layer often need high-temperature sintering to form the ideal crystallization, which is not compatible with the fabrication of PSCs. So most inorganic materials were synthesized into nanoparticles with a good crystallization and then deposited on the perovskite film with a much lower annealing temperature. The compact ETLs on the perovskite film can block the invasion of moisture and prevent the escape of the MA gas from the decomposition of perovskite, as shown in Figure 4a. Therefore, it can stabilize the performance of PSCs.

Most of SnO<sub>2</sub> films are prepared at the temperature more than 150 °C while the perovskite film can be decomposed easily at this temperature. Seeking a much lower-temperature SnO<sub>2</sub> deposition method is vital to the inverted-structure PSCs. Zhu et al. utilized two different methods to prepare the SnO<sub>2</sub> nanocrystals as the precursor of the ETL.<sup>[123]</sup> The methods were hydrolysis sol–gel synthesis and hydrothermal synthesis. For the hydrolysis so–gel synthesis method, the precursor solution was prepared by

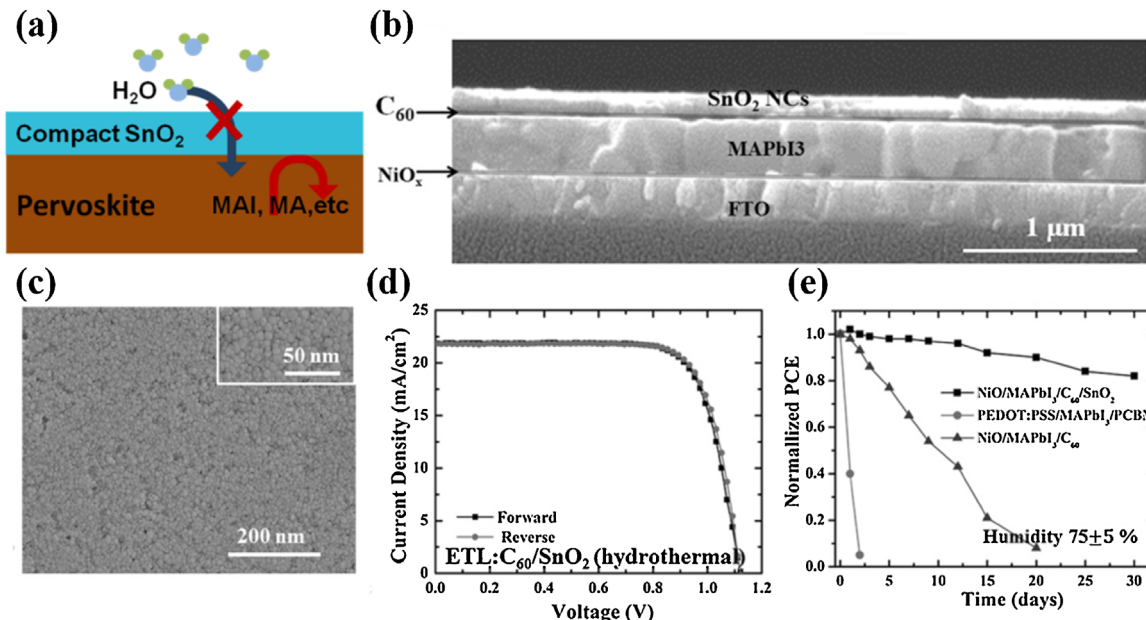


**Figure 4.** a) Schematic diagram for how inverted PSCs improve stability. b) Cross-section SEM image of inverted structure PSCs based on SnO<sub>2</sub>, c) surface SEM image of SnO<sub>2</sub> film, d) different scanning directions *J*–*V* curves of champion PSCs based on SnO<sub>2</sub>, and e) the stability test of PSCs with different structure as a function of storage time in ambient with relative humidity of 75% ± 5%. Reproduced with permission.<sup>[123]</sup> Copyright 2016, Wiley-VCH.

adding  $\text{SnCl}_4 \cdot 5\text{H}_2\text{O}$  (0.350 g, 1.00 mmol) and aqueous TMAH (1.00 m, 8.00 mL) successively into ethanol under intense ultrasonic treatment. The sol-gel  $\text{SnO}_2$  nanocrystals were obtained after the solution was heated at 100 °C for 12 h. For the hydrothermal synthesis method, the solution was prepared by the same way as the hydrolysis. Then the solution was transferred into a Teflon-lined stainless autoclave and kept at 200 °C for 12 h. After the nanocrystals were synthesized, the product was centrifuged and then dispersed into isopropyl alcohol. The  $\text{SnO}_2$  nanocrystals dispersion solution was spin-coated onto the perovskite film on NiO film without any annealing treatment and a compact  $\text{SnO}_2$  film was obtained. Then the silver film was evaporated onto the  $\text{SnO}_2$  film as the contact and the complete device was fabricated. The structure is shown in Figure 4b. The fullerene was used as the interface modification material. The surface SEM showed that  $\text{SnO}_2$  film was compact, as shown in Figure 4c. The corresponding  $J$ - $V$  curves are shown in Figure 4d. The stability test of PSCs based on different structures at high humid condition ( $75 \pm 5\%$ ) in Figure 4e showed that compact  $\text{SnO}_2$  film on perovskite increased the stability of the inverted-structure PSCs. As demonstrated above, using ALD to deposit  $\text{SnO}_x$  can also lower the deposition temperature to below 100 °C, which is compatible with the fabrication process of inverted PSCs. Brinkmann et al. deposited  $\text{SnO}_x$  film on aluminum-doped zinc oxide (AZO) nanoparticle film via low-temperature ALD at 80 °C as the bilayer ETL of inverted PSCs.<sup>[136]</sup> The  $\text{SnO}_x$  on AZO was dense, conformal and pinhole-free layers. It blocked the invasion of the

water molecules from air and also limited the escape of by-product generated from decomposition of perovskite when perovskite film was heated on a hotplate. Stability test results of PSCs based on different ETLs clarified that  $\text{SnO}_x$  on AZO not only improved the photovoltaic performance but also enhanced the stability.

#### 2.4. Flexible Solar Cells

Although the certified PCE of rigid substrate-based PSCs are comparable to the silicon solar cells and have a simple fabrication process, it is still difficult to replace the silicon solar cells to provide the electric power for society due to its short lifetime and difficulty in large-scale manufacture. However, PSCs have an obvious advantage in flexibility. The light-harvester layer has high optical absorption coefficient, and a less than 500 nm of light-harvester layer can absorb most of visible light. The thin light-harvester layer makes PSCs compatible with flexible solar cells. The flexible PSCs often use flexible plastic film as the substrate, which is different from the rigid PSCs. The common used substrates of the flexible PSCs are polyethylene terephthalate (PET) and polyethylene naphthalate (PEN).<sup>[76,77,140–144]</sup> The architecture of flexible PSCs is shown in Figure 5a. These flexible substrates cannot bear the high temperature and the most used methods to fabricate perovskite layer do not need more than 100 °C. Consequently, most of the researches on flexible PSCs are focused on the preparation of the

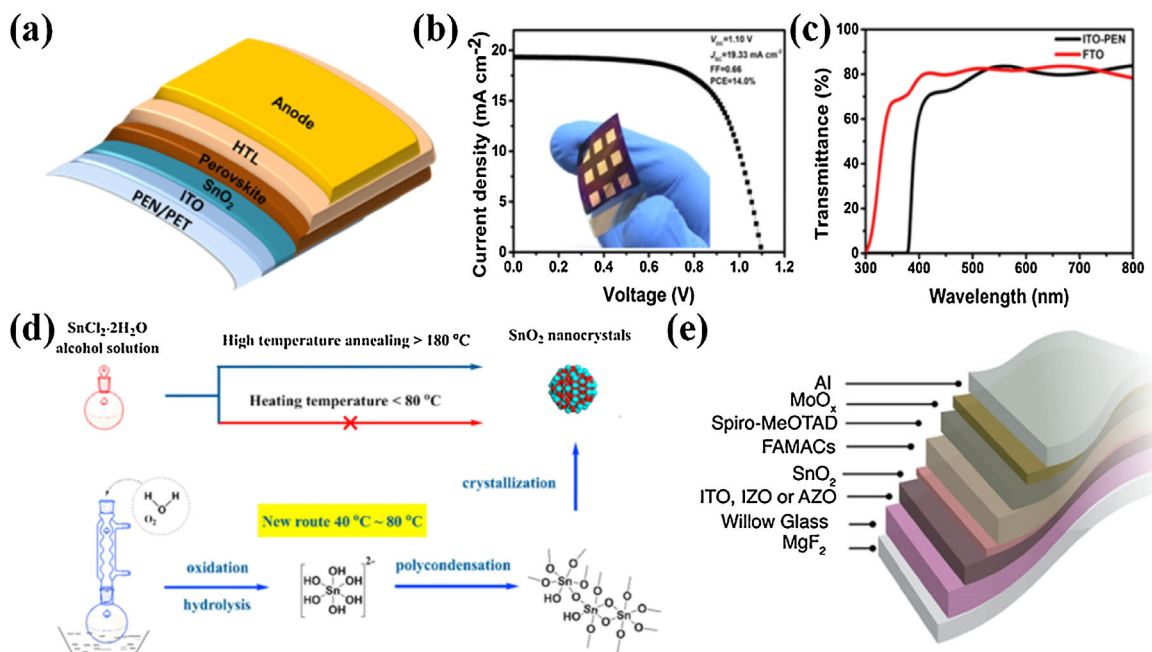


**Figure 5.** a) Structure diagram of flexible PSCs based on  $\text{SnO}_2$ . b)  $J$ - $V$  curves and photovoltaic performance of flexible PSCs based on  $\text{SnO}_2$  deposited by pulse laser deposition (PLD) technique, c) transmission spectra of ITO-PEN and FTO substrates. Reproduced with permission.<sup>[119]</sup> Copyright 2017, Elsevier. d) Schematic diagram of the wet chemical route to synthesize  $\text{SnO}_2$  nanocrystals. Reproduced with permission.<sup>[149]</sup> Copyright 2017, Elsevier. e) Structure diagram of flexible PSCs with a configuration of willow glass/TCO/( $\text{SnO}_2$  ETL)/CsMAFA/Spiro-OMeTAD/ $\text{MoO}_x$ /Au (TCO refers to transparent conductive oxide, such as ITO, IZO, or AZO). Reproduced with permission.<sup>[151]</sup> Copyright 2017, American Chemical Society.

charge transport layer to lower the fabrication temperature in the whole process. There are a lot of materials suitable for fabrication of flexible solar cells. The ETL materials for flexible solar cells including phenyl-C61-butyric acid methyl ester (PCBM), fullerene, 1-benzyl-3-methylimidazolium chloride, ZnO, SnO<sub>2</sub>, and Nb<sub>2</sub>O<sub>3</sub>.<sup>[58,59,77,85,119,140,144–146]</sup> Among these materials, SnO<sub>2</sub> shows many merits such as low cost, high-optical transmission, and high-electron mobility.

Although SnO<sub>2</sub> can be prepared at much lower temperature compared with TiO<sub>2</sub>, the temperature of the frequently used solution methods to deposit SnO<sub>2</sub> reported in refs.<sup>[14,97]</sup> was still higher than 150 °C and the serious deformation of substrate was happened at 150 °C. The plastic substrates were in favor of the temperature lower than 150 °C. Using low-temperature vapor deposition methods, including physical vapor deposition and chemical vapor deposition, fabricating SnO<sub>2</sub> at low temperature is a promising method. Chen et al.<sup>[119]</sup> using a PLD method to deposit the SnO<sub>2</sub> as the ETL for PSCs. They found that the SnO<sub>2</sub> film prepared at room temperature also showed efficient electron transport, so they used PLD method to deposit SnO<sub>2</sub> onto ITO-PEN substrate and fabricated flexible PSCs. The champion flexible PSCs showed a high PCE of 14.0% with a V<sub>OC</sub> of 1.10 V, a J<sub>SC</sub> of 19.33 mA cm<sup>-2</sup>, and a FF of 66%. The J-V curves and photograph of flexible PSCs were shown in Figure 5b and the inset of Figure 5b, respectively. The declined performance was attributed to the lower light transmittance of ITO-PEN compared with FTO glasses, as shown in Figure 5c. The ALD is one of the advanced methods to deposit thin compact metal oxide films. The deposition temperature of thermal ALD is within 200–300 °C. To lower the deposition temperature, ozone and oxygen plasma are introduced as the oxygen precursor source. Wang et al. deposited SnO<sub>2</sub> ETLs for flexible PSCs by plasma enhanced ALD (PEALD) at 100 °C.<sup>[118]</sup> The champion flexible PSCs achieved a PCE of 16.80% with a V<sub>OC</sub> of 1.11 V, a J<sub>SC</sub> of 20.50 mA cm<sup>-2</sup>, and a FF of 69.28%. The flexible PSCs also showed good flexibility endurance. The performance of the flexible PSCs still retained approximately 85 % of its initial PCE after 200 times of bending with a minimum radius of curvature of 5 mm, indicating good flexibility endurance of the flexible PSCs with the low-temperature PEALD SnO<sub>2</sub> ETL. Wang et al. also used plasma enhanced ALD to deposit the SnO<sub>2</sub> film as the ETLs of flexible PSCs.<sup>[146]</sup> Then they deposited a C<sub>60</sub>-self-assembled monolayer (C<sub>60</sub>-SAM) on PEALD SnO<sub>2</sub> to modify the interface between perovskite and SnO<sub>2</sub>. They focused their research on the composition and morphology of the mixed cation perovskite film (MA<sub>1-x</sub>FA<sub>x</sub>PbI<sub>3</sub>). They adjusted the ratio of MA and FA firstly to optimize the composition of perovskite. Moreover, they added a small amount of lead thiocyanate additive into the mixed perovskite to enlarge the grain size. Flexible PSCs with the best PCE of 17.96% were obtained. Although using oxygen plasma as the oxygen source can lower the deposition temperature, the flexible solar cells suffered from a lower V<sub>OC</sub>, FF, and a higher degree of J-V hysteresis in comparison with the control devices fabricated on rigid substrates.<sup>[118]</sup> These issues resulted from the residue of impurities and post-deposition treatment improved the conductivity of low-temperature PEALD-processed SnO<sub>2</sub> ETLs.<sup>[147]</sup> Therefore, Wang et al. treated PEALD-synthesized SnO<sub>2</sub> ETLs with water vapor at 100 °C.<sup>[148]</sup> It was found that the water vapor

treatment at 100 °C improved the electrical conductivity of SnO<sub>2</sub> ETLs. The reason was that annealing with water vapor facilitated the complete reaction of organic materials and lead to the formation of purer SnO<sub>2</sub>. The flexible PSCs with a structure of PET/ITO/SnO<sub>2</sub>/C60-SAM/perovskite/spiro-OMeTAD/Au were fabricated. The champion flexible PSCs obtained a PCE of 18.36% (17.12%) measured under reverse (forward) voltage scan and a stabilized efficiency over 17%.

Besides vapor deposition, synthesizing SnO<sub>2</sub> nanoparticles as the precursor of ETL is also an effective way to deposit SnO<sub>2</sub> at low temperature. For the conventional solution route, the crystallized SnO<sub>2</sub> is formed after the solution is spin-coated and thermally annealed. Synthesizing SnO<sub>2</sub> nanocrystals prior to spin coating can avoid that the plastic substrates are annealed at high-temperature. Dong et al. used wet chemical route to synthesize SnO<sub>2</sub> nanocrystals as ETL material for PSCs.<sup>[149]</sup> The SnO<sub>2</sub> nanocrystals were synthesized as following process, as shown in the new route of Figure 5d. The SnCl<sub>2</sub> · H<sub>2</sub>O was dissolved into anhydrous alcohol in flask to prepare SnCl<sub>2</sub> · H<sub>2</sub>O solution. Then the just dissolved solution was transferred to an open reflux apparatus and refluxed the solution for different time at different temperature, respectively. The participation of atmosphere O<sub>2</sub> and H<sub>2</sub>O by refluxing can greatly promote oxidation and hydrolysis of Sn<sup>2+</sup> in SnCl<sub>2</sub> · H<sub>2</sub>O alcohol solution. When the reaction was over, the resulted product was aged for over 24 h at room temperature. It was found that the increase of particle size was caused by rising refluxing temperature. They found that the new route was applicable to low-temperature fabrication of SnO<sub>2</sub> ETL and had a promising application in flexible PSCs. Based on SnO<sub>2</sub> ETLs, rigid and flexible PSCs attained the highest PCE of 19.2% and 16.11%, respectively. Yang et al. used two-step low-temperature method to synthesize and control the carrier concentration of colloidal SnO<sub>2</sub> QDs.<sup>[116]</sup> Because of the low-temperature process ability of the SnO<sub>2</sub> QDs, they fabricated the flexible PSCs with a configuration of PEN/ITO/(SnO<sub>2</sub> QDs ETL)/ CsMAFA/Spiro-OMeTAD/Au. The champion flexible PSCs showed a PCE of 16.97% (15.24%) measured under reverse (forward) voltage scan. Jiang et al. has shown that state-of-the-art planar PSCs can be obtained via using smaller-scale SnO<sub>2</sub> nanoparticles (ca. 3–4 nm) which was dispersed in water as the precursor of ETL.<sup>[102]</sup> However, the annealing temperature of SnO<sub>2</sub> is 150 °C and it is not suitable for fabrication of plastic flexible PSCs. The ultra-thin glass (willow glass) can withstand the processing temperature up to 700 °C and block the invasion of the water molecules. Willow glass has been used as the substrate material of flexible PSCs by Tavakoli et al.<sup>[150]</sup> Dou et al. used willow glass as the flexible substrate and SnO<sub>2</sub> nanoparticles reported in ref.<sup>[102]</sup> as the ETL material.<sup>[151]</sup> They used different TCOs as the anode electrode of flexible solar cells, as shown in Figure 5e. Flexible PSCs based on indium zinc oxide (IZO) showed the best performance among the flexible PSCs with different TCOs as the anode electrode due to the stoichiometry change of the perovskite film surface. The flexible PSCs with a PCE of 18.1% was obtained.

### 3. Enhancing Performance of PSCs

Although SnO<sub>2</sub> has shown irreplaceable advantages, it still suffers from some problems. Like many other metal oxides, e.g.,

$\text{TiO}_2$ , the  $\text{SnO}_2$  film also contains bulk and surface defects, which could capture charge carriers and deteriorate the electronic properties. It was clarified that defects mainly came from the oxygen vacancies.<sup>[152]</sup> High-temperature annealing was an effective method to eliminate the vacancies. However, the performance of PSCs degraded after the  $\text{SnO}_2$  film had been treated with high temperature annealing process.<sup>[97]</sup> To settle these issues, a lot of work has been carried out, including doping  $\text{SnO}_2$  with other elements and modifying the surfaces of  $\text{SnO}_2$ .

### 3.1. Control Morphology of $\text{SnO}_2$

Zhao et al. found that the  $\text{SnO}_2$  films prepared by the solution based method began to aggregate and did not completely cover the FTO substrates after high-temperature annealing treatment, resulting in serious charge recombination.<sup>[97]</sup> To address this issue, they attempted to introduce magnesium (Mg) into the  $\text{SnO}_2$  films to inhibit the aggregation.<sup>[153]</sup>  $\text{Mg}^{2+}$  has an ionic radius of 72 nm, and it is close to the ionic radius of  $\text{Sn}^{4+}$ . They added  $\text{Mg}(\text{CH}_3\text{COO})_2 \cdot 4\text{H}_2\text{O}$  into the  $\text{SnCl}_2 \cdot 2\text{H}_2\text{O}$  solution and mixed them to prepare the precursor solution of Mg-doped  $\text{SnO}_2$  films. After the spin-coating of the solution, all samples were heated at 550 °C. The XRD patterns of Mg-doped  $\text{SnO}_2$  showed that the incorporation of Mg ions into the  $\text{SnO}_2$  film did not affect the crystal lattice dramatically. The top surface morphology of the  $\text{SnO}_2$  films undoped and doped with  $\text{Mg}^{2+}$  was shown in Figure 6a,b, respectively. The pristine  $\text{SnO}_2$  film was discontinuous owing to the appearance of many cracks, indicating that  $\text{SnO}_2$  materials cannot cover the FTO substrate completely. After Mg doping, the morphology of  $\text{SnO}_2$  film changed dramatically and appropriate Mg doping significantly improved the film quality. Doping  $\text{SnO}_2$  with Mg did not affect the transmittance spectrum of the  $\text{SnO}_2$  film. To determine whether doping in  $\text{SnO}_2$  was feasible for the improvement of device performance, MAPbI<sub>3</sub> PSCs based on doped and undoped  $\text{SnO}_2$  films were

fabricated. The  $J$ - $V$  curves and stabilized power output of devices were shown in Figure 6c,d, respectively. The statistical data of the device performance demonstrated that Mg doping in  $\text{SnO}_2$  films influenced the photovoltaic performance dramatically. Employing the optimum Mg content (7.5%) could achieve a nearly 89% enhancement (from 7.16% to 13.56%) in the average PCE of the devices, due to the improved morphology and electron mobility of the Mg-doped  $\text{SnO}_2$ .

Doping  $\text{SnO}_2$  with other metal elements can not only enhance the continuity of  $\text{SnO}_2$  films, but also facilitate the generation of micro-nano structures like nanosheets. Micro-nano structures can increase the surface-to-volume ratio of ETL, and moderate dopants can also enhance the conductivity of ETL, so that it can boost the extraction of the electrons from perovskite films.

Yang et al. used the hydrothermal method to synthesize yttrium (Y)-doped  $\text{SnO}_2$  nanosheets and then form  $\text{SnO}_2$  films.<sup>[154]</sup> The precursor solution was prepared by dissolving equimolar tin oxalate powder and hexamethylenetetramine in DI water. For the Y-doped  $\text{SnO}_2$  films, a small amount of yttrium(III) nitrate hexahydrate ( $\text{Y}(\text{NO}_3)_3 \cdot 6\text{H}_2\text{O}$ ) was added into the  $\text{SnO}_2$  precursor solution. Both the precursor solutions were stirred under ambient conditions for 1 h. These two precursor solutions together with FTO glasses were put into two different ovens and the hydrothermal growth was conducted at 95 °C for 9 h. The process is shown in Figure 6e. The films prepared by the different precursor solutions were shown in Figure 6f,g. XRD patterns showed that no phase impurity related to Y appeared. The peak positions of Y- $\text{SnO}_2$  films tended to shift towards higher angles and the peaks broadened slightly, so the  $\text{Y}^{3+}$  ions were incorporated into  $\text{SnO}_2$  films without degrading the structure quality of  $\text{SnO}_2$  films. From the SEM images of  $\text{SnO}_2$  films, it was found that Y doping could promote the formation of the well-aligned and homogeneously distributed  $\text{SnO}_2$  nanosheets. The transmittance spectra of FTO substrates coated with  $\text{SnO}_2$  and Y-doped  $\text{SnO}_2$  films clarified that both the doped and the undoped  $\text{SnO}_2$  films could improve the optical transmission of FTO

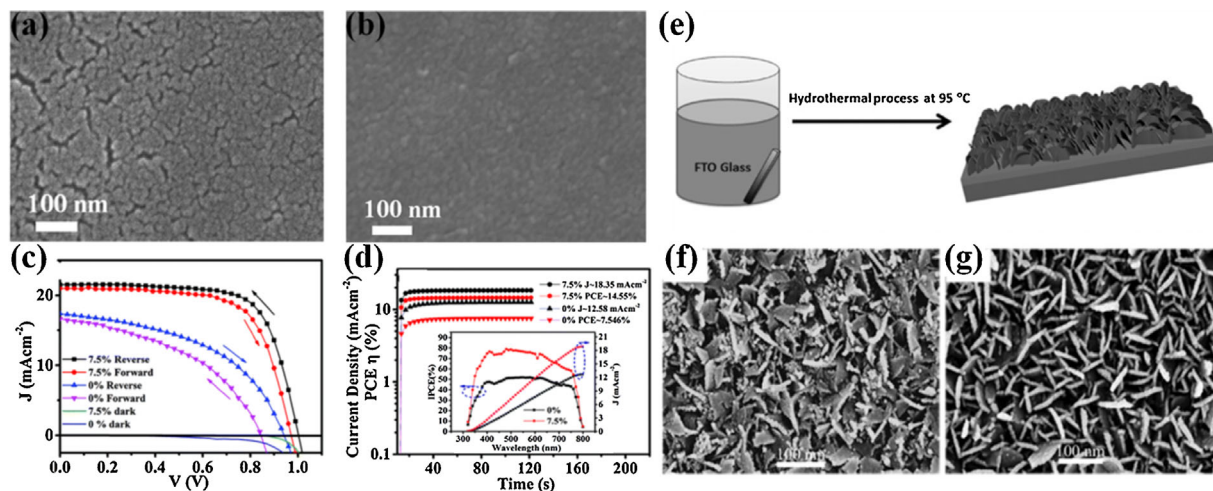


**Figure 6.** a,b) SEM images of  $\text{SnO}_2$  doped with a) 0, b) 7.5 mol% Mg, c)  $J$ - $V$  curves of PSCs measured under AM 1.5G condition with input solar power of  $100 \text{ mW cm}^{-2}$ , d) steady-state efficiency of the PSCs and integrated photocurrent density  $J_{\text{SC}}$  of IPCE spectra for PSCs (inset). Reproduced with permission.<sup>[153]</sup> Copyright 2013, Royal Society of Chemistry. e) Schematic diagram of hydrothermal process to prepare  $\text{SnO}_2$  and Y- $\text{SnO}_2$  thin films on FTO, f,g) top view SEM images of the  $\text{SnO}_2$  thin film f) and the Y- $\text{SnO}_2$  thin film g). Reproduced with permission.<sup>[154]</sup> Copyright 2016, Wiley-VCH.

substrates.  $\text{CH}_3\text{NH}_3\text{PbI}_3$  perovskites and Spiro-OMeTAD films were spin-coated onto substrates sequentially. Finally, the 80 nm gold film was deposited onto the HTL. The photovoltaic performance of the PSCs with  $\text{SnO}_2$  and Y-doped  $\text{SnO}_2$  ETLs was investigated under simulated one-sun illumination. The devices using the Y-doped  $\text{SnO}_2$  ETL performed much better than the devices using the pristine  $\text{SnO}_2$  ETL. All the figures of merits of the devices based on the Y-doped  $\text{SnO}_2$  films had been improved. The fill factor of cells using the Y-doped  $\text{SnO}_2$  exhibited an obviously higher value than that of cells using the undoped  $\text{SnO}_2$  due to the improved interfacial connection between  $\text{SnO}_2$  ETLs and perovskite absorbers. The conductivity measurement also showed that doping  $\text{SnO}_2$  with moderate Y could enhance conductivity. The enhanced conductivity facilitated the electron transport in ETL, resulting in the improved  $J_{\text{SC}}$ . To identify the reasons for the improvement of the  $V_{\text{OC}}$ , UPS was carried out. The Fermi levels of  $\text{SnO}_2$  and Y-SnO<sub>2</sub> films were 5.19 eV and 5.11 eV, respectively. The  $E_f - E_V$  of  $\text{SnO}_2$  and Y-SnO<sub>2</sub> were both 2.88 eV. The band gaps of  $\text{SnO}_2$  and Y-SnO<sub>2</sub> films were also calculated. The band gaps of  $\text{SnO}_2$  and Y-SnO<sub>2</sub> films were 3.65 eV and 3.70 eV, respectively. Therefore, the calculated conduction band minimum (CBM) of Y-SnO<sub>2</sub> was 0.13 eV higher than that of  $\text{SnO}_2$ . The value of  $|E_{\text{CBM}} - E_f|$  for Y-SnO<sub>2</sub> was larger than that of  $\text{SnO}_2$ , indicating a lower concentration of electrons in conduction band (CB) of Y-SnO<sub>2</sub> compared with pristine  $\text{SnO}_2$  and thus resulting in a reduced interface recombination. Both the lower WF and lower concentration of electrons in CB contributed to the higher  $V_{\text{OC}}$ .

### 3.2. Eliminate Bulk Defects of $\text{SnO}_2$ Films

$\text{SnO}_2$  showed different electrical properties when the ratio between tin and oxygen was different. Oxygen-deficient form  $\text{SnO}_2$  behaved as the donor-type semiconductor. However, the stoichiometrically formed  $\text{SnO}_2$  acts as the insulator, not favorable for ETL materials of PSCs. When the oxygen was extremely rich, localized oxygen holes appeared. The oxygen holes did not play as charge carriers but tended to pair up to form peroxide ions. The peroxide ions acted as charge traps in  $\text{SnO}_2$  films, also not favorable for electron transport. The oxygen contents of  $\text{SnO}_2$  films were related to the deposition conditions strongly.<sup>[155]</sup> To reduce the formation of peroxide ions, the excess oxygen must be consumed when  $\text{SnO}_2$  was formed under the oxygen-rich condition. A good method to consume oxygen was doping  $\text{SnO}_2$  film with metal elements possessing higher oxidation states. The dopant metal elements often had more than 4 electrons at the outside electron orbits and can provide excess free electrons when incorporated into crystal structures of  $\text{SnO}_2$ . These free electrons acted as the carrier charges and also filled the charge traps, thus, the new metal element brought about the enhanced free charge concentration. The Fermi level of ETL was closely related to the carrier concentration according to the Equation (1).

$$\frac{n_2}{n_1} = \exp\left(\frac{E_{f2} - E_{f1}}{kT}\right) \quad (1)$$

where  $n_2$  and  $n_1$  are the carrier concentrations of the pristine and the doped  $\text{SnO}_2$ , respectively.  $E_{f1}$  and  $E_{f2}$  are the Fermi levels of the pristine and the doped  $\text{SnO}_2$ , respectively.  $k$  is the boltzmann constant, and  $T$  is the temperature. The higher free charge concentration and the less traps led to the higher Fermi level and the lower work function value, as shown in Figure 7a. ETLs with the lower work function values were in favor of the extraction charges from perovskites and resulted in a higher  $V_{\text{OC}}$ , as shown in Figure 7b.

Bai et al. introduced Sb into  $\text{SnO}_2$  films to increase the charge density and lower the defect density. Dopants in  $\text{SnO}_2$  did not affect the light transmittance of ETLs.<sup>[156]</sup> The conductivity measurement showed that the conductivity of Sb-doped  $\text{SnO}_2$  dramatically increased over one order of magnitude compared with pristine  $\text{SnO}_2$ , which may arise from the higher carrier concentration, as illuminated in Figure 7c. To identify the doping effects on depth and verify the significantly improved electrical conductivity, they constructed N-I-P planar PSCs with a structure of ITO/ $\text{SnO}_2$  or Sb: $\text{SnO}_2$  ETL/perovskite/HTL/Au. The carrier concentrations of doped and undoped films were both measured by Hall effect measurement. The carrier concentration of ETLs increased from  $6.7 \times 10^{21}$  to  $8.2 \times 10^{22} \text{ m}^{-3}$  and the Fermi level was upward shifted for 60 meV after doping according to the Equation (1). The up-shifted Fermi level was expected to increase the  $V_{\text{OC}}$  of the solar cells. To confirm the expectation, complete solar cells based on  $\text{MAPbI}_3$  perovskite films were fabricated. The  $J$ - $V$  curves for different scanning directions were measured to characterize the photovoltaic performance. The reference device measured under the reverse (forward) scanning direction had a  $V_{\text{OC}}$  of 1.01 V (1.00 V), a  $J_{\text{SC}}$  of  $22.3 \text{ mA cm}^{-2}$  ( $22.1 \text{ mA cm}^{-2}$ ), a FF of 69.6% (59.7%), and a PCE of 15.7% (13.2%), and exhibited significant hysteresis. Comparatively, the target device measured under the reverse (forward) scanning direction showed a  $V_{\text{OC}}$  of 1.06 V (1.06 V), a  $J_{\text{SC}}$  of  $22.6 \text{ mA cm}^{-2}$  ( $22.5 \text{ mA cm}^{-2}$ ), and a FF of 72.0% (67.8%), yielding a PCE of 17.2% (16.2%). The  $J$ - $V$  curves for different scanning directions showed less hysteresis. The higher  $V_{\text{OC}}$  of the target device was in consistent with the higher Fermi level and the higher FF and  $J_{\text{SC}}$  of the target device was also consistent with the better conductivity.

Ren et al. doped  $\text{SnO}_2$  with Nb whose outer orbits also contained 5 electrons. The precursor solutions were prepared by dissolving  $\text{SnCl}_2 \cdot 2\text{H}_2\text{O}$  in ethanol.<sup>[100]</sup> The Nb-doped  $\text{SnO}_2$  precursor solutions were prepared by adding niobium ethoxide into the  $\text{SnCl}_2 \cdot 2\text{H}_2\text{O}$  solution. The  $\text{SnO}_2$  films were deposited by spin-coating the precursor solution onto substrates followed by thermal annealing at 190 °C for 1 h. The XRD patterns indicated that the  $\text{SnO}_2$  films remained the rutile phase irrespective of the Nb doping, although the (111) rutile peak slightly shifted to the smaller  $\theta$  angle with increased Nb doping content, which was due to the bigger ionic radius of  $\text{Nb}^{5+}$  in comparison with  $\text{Sn}^{4+}$ . Both the pristine  $\text{SnO}_2$  films and the doped  $\text{SnO}_2$  films were flat, uniform and pinhole-free, which were beneficial to the high photovoltaic performance. The electrical conductivity measurement in Figure 7d showed that electrical conductivity of the  $\text{SnO}_2$  films was improved significantly with the increased Nb composition. The dark  $J$ - $V$  curves for electron-only devices were used to calculate the electron trap-state density in the  $\text{SnO}_2$  and the Nb-doped  $\text{SnO}_2$ .

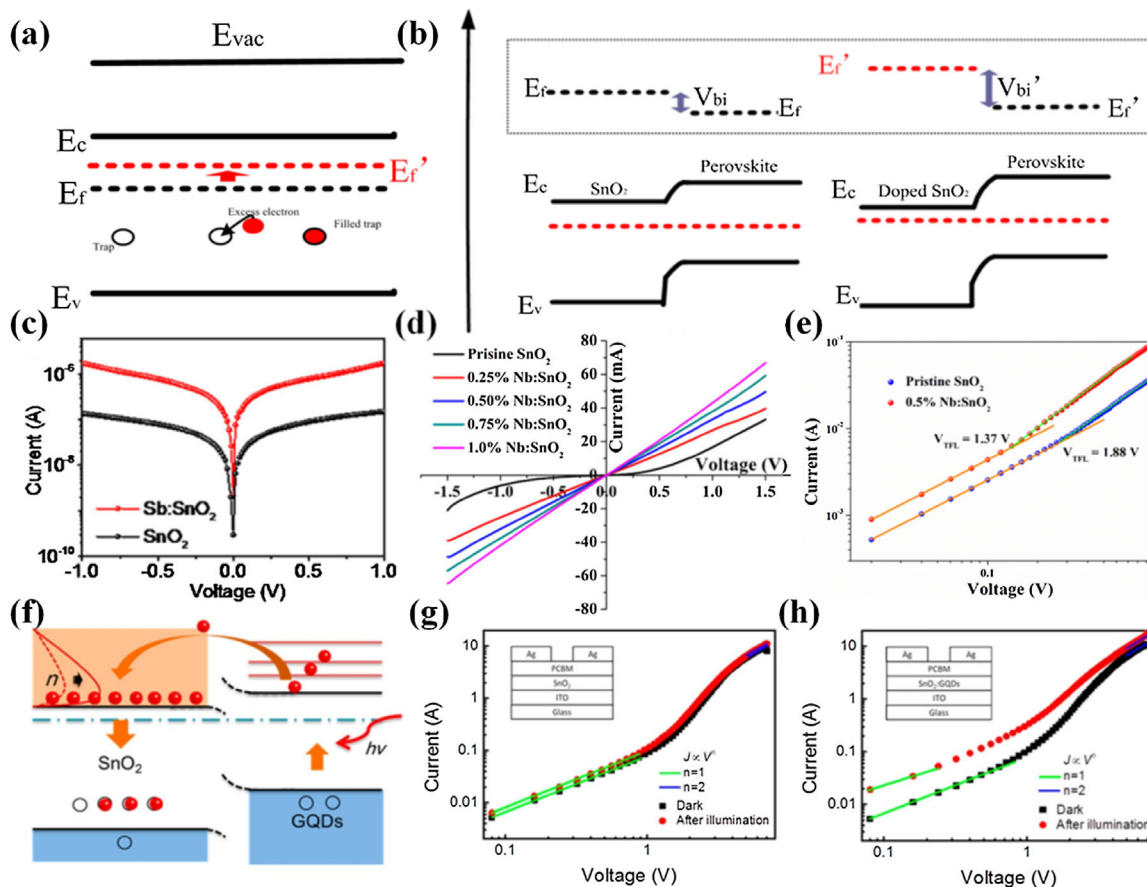


**Figure 7.** a) Change of Fermi energy level after traps were filled, b) schematic illustration of the band diagram in equilibrium, showing the formation of the  $\text{SnO}_2$ (doped  $\text{SnO}_2$ )/perovskite heterojunction (initial Fermi levels of  $\text{SnO}_2$ , doped  $\text{SnO}_2$  and perovskite films before contact were shown in the dashed dot area,  $V_{\text{bi}}$  stands for the in-built voltage). c)  $I$ - $V$  curves of the  $\text{SnO}_2$  and the  $\text{Sb}:\text{SnO}_2$  NC films deposited on glass substrates. Reproduced with permission.<sup>[156]</sup> Copyright 2016, Wiley-VCH. d)  $I$ - $V$  curves of the  $\text{SnO}_2$  and the  $\text{Nb}:\text{SnO}_2$  films with different Nb contents, e) Dark  $I$ - $V$  curves of the electron-only device, revealing  $V_{\text{TFL}}$  kink point behavior. Reproduced with permission.<sup>[100]</sup> Copyright 2017, American Chemical Society. f) The schematic of the electrons transferring from GQDs to  $\text{SnO}_2$  under illumination, g)  $I$ - $V$  curves of the electron only device with the configuration shown in the inset under dark and after illumination, h)  $I$ - $V$  curves of the electron only device with the configuration shown in the inset under dark and after illumination. Reproduced with permission.<sup>[152]</sup> Copyright 2017, American Chemical Society.

films, as shown in Figure 7e. The linear relationship indicated the ohmic response of the electron-only device at the low bias voltage. When the bias voltage exceeded the kink point, the current quickly increased nonlinearly, which demonstrated that the trap states were completely filled. The trap density was calculated by Equation (2),

$$V_{\text{TFL}} = \frac{en_t L^2}{2\epsilon\epsilon_0} \quad (2)$$

where  $e$  is the elementary charge of the electron,  $L$  is the thickness of the undoped  $\text{SnO}_2$  or Nb-doped  $\text{SnO}_2$  film,  $\epsilon$  is the relative dielectric constant of the  $\text{SnO}_2$ ,  $\epsilon_0$  is the vacuum permittivity, and  $n_t$  is the trap-state density. The  $V_{\text{TFL}}$  could be gained from the kink point in the  $I$ - $V$  curve. The  $V_{\text{TFL}}$  for pristine  $\text{SnO}_2$  (1.88 V) was higher than that for the Nb doped  $\text{SnO}_2$  (1.37 V). Consequently, the Nb-doped  $\text{SnO}_2$  films had a much lower electron trap density. Clearly, dopants had effectively passivated the electron traps. The transmittance demonstrated

that doping Nb in  $\text{SnO}_2$  did not affect the transmission of  $\text{SnO}_2$  films. PSCs based on  $(\text{FAPbI}_3)_{0.85}(\text{MAPbBr}_3)_{0.15}$  perovskites were fabricated. The  $J$ - $V$  curves of PSCs under the reverse and forward scanning directions demonstrated that doping  $\text{SnO}_2$  with Nb could improve the photovoltaic performance of PSCs. PSCs based on the Nb:SnO<sub>2</sub> films had the best PCE of 17.57% for the reverse scan and 12.75% for the forward scan. In comparison, PSCs based on the pristine  $\text{SnO}_2$  films possessed the best PCE of 15.13% and 11.12% for the reverse and forward scans, respectively.

The excess electrons in  $\text{SnO}_2$  films could also be provided by QDs like graphene QDs (GQDs) apart from doping the above atoms. Xie et al. doped  $\text{SnO}_2$  films with GQDs. The GQDs were dispersed in water first and then the graphene dispersion was added into the  $\text{SnCl}_2 \cdot 2\text{H}_2\text{O}$  ethanol solution.<sup>[152]</sup> The final  $\text{SnO}_2$  films were prepared through spin-coating the solution onto the ITO glass followed by annealing in air at 180 °C. The transmission spectra of  $\text{SnO}_2$  and  $\text{SnO}_2$ : GQDs showed that the transmission of the  $\text{SnO}_2$ : GQDs films was slightly lower in

the range of 300–550 nm and similar in the range of 550–900 nm in comparison with that of the pristine  $\text{SnO}_2$  films, due to the absorption of GQDs with a band gap of  $\approx 2.4$  eV. To identify the role of the GQDs in the  $\text{SnO}_2$  films, the ITO/ $\text{SnO}_2$ (GQDs)/Ag architecture was used to study the conductivity of the  $\text{SnO}_2$ . The conductivity of the  $\text{SnO}_2$ :GQDs thin films increased dramatically and had a  $\approx 20$  times improvement compared with the films in the dark. However, the conductivity of the bare  $\text{SnO}_2$  showed the slight improvement under the illumination. The conductivity of the  $\text{SnO}_2$  films could be expressed as  $\sigma = q \times n \times u$ , where  $q$  is the elementary charge,  $n$  is the number of electrons, and  $u$  is the electron mobility. The UPS and optical absorption were measured to determine the CB and valence band of different materials. The energy band alignment between  $\text{SnO}_2$  and GQDs was shown in Figure 7f. After illumination, the charge carriers would be generated in GQDs and transferred into  $\text{SnO}_2$ . The transferred electrons would fill the electron traps in  $\text{SnO}_2$ . Kelvin probe force microscope measurement results showed that the  $E_f$  of the  $\text{SnO}_2$ :GQDs decreased from 4.35 eV to 4.01 eV after illumination, indicating that the electron concentration in the  $\text{SnO}_2$ :GQDs increased through illumination according to the Equation (1). In comparison, the  $E_f$  of the bare  $\text{SnO}_2$  showed much less reduction and the variation quantity was only 0.08 eV. The trap density and carrier mobility were obtained by the space charge limited current technique (SCLC). The SCLC results of the electron-only devices were shown in Figure 7g,h. The electron trap density was calculated by the Equation (1) and the electron mobility was obtained according to Mott–Gurney law:

$$J = \frac{9\epsilon\epsilon_0\mu V_b^2}{8L^3} \quad (3)$$

where  $V_b$  is the applied voltage. The  $V_{\text{TFL}}$  results showed that the electron trap-state density of the  $\text{SnO}_2$ :GQDs was reduced from  $4.30 \times 10^{16}$  to  $1.23 \times 10^{16} \text{ cm}^{-3}$  after illumination, while the value for the bare  $\text{SnO}_2$  showed negligible decrease. The mobility results showed that the electron mobility of the  $\text{SnO}_2$ :GQDs had been improved dramatically after illumination due to the decreased electron trap-state density. The N-I-P PSCs with the structure of ITO/ $\text{SnO}_2$ (GQDs)/ $\text{CH}_3\text{NH}_3\text{PbI}_3$ /Spiro-OMe-TAD/Au were fabricated. The devices fabricated on the  $\text{SnO}_2$ :GQDs exhibited better performance than those on the bare  $\text{SnO}_2$  for all the photovoltaic parameters. The average  $V_{\text{OC}}$  increased from  $1.09 \pm 0.02$  V to  $1.12 \pm 0.02$  V with the GQDs, the average  $J_{\text{SC}}$  increased from  $21.58 \pm 0.50 \text{ mA cm}^{-2}$  to  $22.56 \pm 0.38 \text{ mA cm}^{-2}$ , and the average FF increased from  $70.1 \pm 2.4\%$  to  $74.7 \pm 2.3\%$ . As a result, the devices based on the  $\text{SnO}_2$ :GQDs exhibited a higher average PCE ( $19.2 \pm 1.0\%$ ) than those on the bare  $\text{SnO}_2$  ( $16.6 \pm 0.9\%$ ). The higher  $V_{\text{OC}}$  of the devices based on the  $\text{SnO}_2$ :GQDs was attributed to the higher  $E_f$  level of the ETLs. The higher FF and  $J_{\text{SC}}$  resulted from the higher conductivity of the  $\text{SnO}_2$ :GQDs under the illumination.

### 3.3. Passivate Interface of $\text{SnO}_2$ -Based PSCs

Although  $\text{SnO}_2$  films have a lot of advantages compared with other metal oxide films, it also has the same interface problems as other metal oxide films when used as the ETL of PSCs. Due to

the mismatch between the metal oxides and perovskite films, there are a lot of defects at the interfaces, degrading the performance of PSCs. Terminal status of metal oxides could also affect the morphology of the perovskite layers. To improve the PV performance, the metal oxide films were often modified by other materials such as fullerene and its derivatives.<sup>[62,134,157]</sup> These materials can passivate the traps at the (metal oxide)/perovskite interfaces and perovskite grain boundaries.<sup>[91]</sup> After the eliminating traps, electrons can be transported unobstructed at the  $\text{SnO}_2$ /perovskite interfaces and perovskite grain boundaries, as shown in Figure 8a.

To promote the electron transfer, Ke et al. introduced the thin PCBM films onto the  $\text{SnO}_2$  films before spin-coating perovskites.<sup>[157]</sup> Figure 8b shows the  $J$ – $V$  curves of the planar PSCs using  $\text{SnO}_2$  and  $\text{SnO}_2$ /PCBM ETLs. PSCs based on the  $\text{SnO}_2$  ETL and the  $\text{SnO}_2$ /PCBM ETL achieved a PCE of 16.53% and 18.17% when measured under the reverse scanning direction, respectively. Obviously, the performance of PSCs using  $\text{SnO}_2$ /PCBM was much better than that of PSCs using  $\text{SnO}_2$ . It showed that  $J_{\text{SC}}$  of PSCs using  $\text{SnO}_2$ /PCBM was slightly higher than that of PSCs using  $\text{SnO}_2$  and was not affected by the PCBM layers. Most of the PCBM could be dissolved into the perovskite solutions and washed away along with them, when the perovskite films were spin-coated onto the substrates. Therefore, the PCBM films between the perovskites and  $\text{SnO}_2$  were very thin, which could not affect the transmission of the light according to the almost identical absorbance spectra of perovskites on different substrates. These results were also testified by EQE spectra which were shown in Figure 8c. The left PCBM in the perovskite films could passivate defects at the boundaries of the perovskite grains. However, the structure characterization revealed that the different ETLs did not cause obvious changes in the morphology of the perovskite layers, revealing that the enhanced performance was induced by the improved ETL/perovskite interface possibly. The time-resolved photoluminescence (TRPL) from the research of Steve Albrecht showed that the PCBM and fullerene layers quenched the photoluminescence signal stronger than metal oxide interfaces, indicating that fullerene and PCBM could transfer electrons more efficiently,<sup>[158]</sup> thus, the PCBM on  $\text{SnO}_2$  could transfer electrons from the perovskite film and then deliver them into  $\text{SnO}_2$ .  $\text{SnO}_2$  could block the holes and reduce the recombination due to the much deeper VBM level compared with PCBM. Combining both the advantages from  $\text{SnO}_2$  and PCBM improved the performance of PSCs ultimately.

Although the PCBM could modify the (metal oxide)/perovskite interfaces, it was easily dissolved by the solvents from the perovskite solutions, resulting in the inhomogeneous PCBM films. Yang et al. introduced the 3-aminopropyltriethoxysilane (APTES) self-assemble monolayer (SAM) as the interfacial layers to modify the  $\text{SnO}_2$  film surfaces.<sup>[159]</sup> After the preparation of the  $\text{SnO}_2$  films, the substrates were immersed into the solution of APTES in isopropanol for several hours to grow the APTES SAM on the  $\text{SnO}_2$  surfaces. The schematic diagram of PSCs based on the SAM modified  $\text{SnO}_2$  ETL was showed in Figure 8d. There were a lot of hydroxyl groups appeared at the surfaces of the  $\text{SnO}_2$  films. The hydroxyl groups could be bonded chemically with the organic hydrolyzed alkoxy via hydrogen-bonding. It was found that the SAM could affect

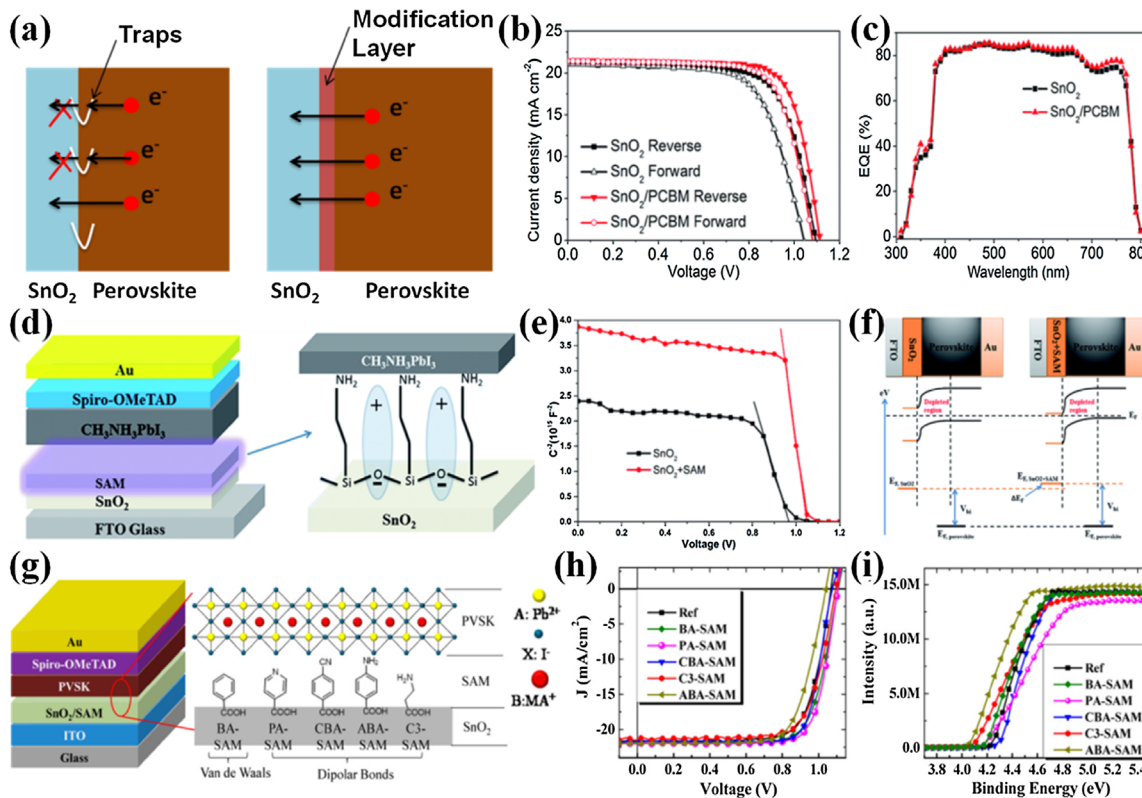


**Figure 8.** a) Electron transferred at  $\text{SnO}_2$  (modified  $\text{SnO}_2$ )/perovskite interface. b)  $J$ - $V$  curves of the PSCs employing  $\text{SnO}_2$  and  $\text{SnO}_2/\text{PCBM}$  ETLs under the different scanning directions, c) EQE spectra of the PSCs using  $\text{SnO}_2$  and  $\text{SnO}_2/\text{PCBM}$  ETLs. Reproduced with permission.<sup>[157]</sup> Copyright 2016, Royal Society of Chemistry. d) Schematic diagram of PSCs based on the APTES modified  $\text{SnO}_2$  ETLs, e) Mott–Schottky analysis at 1 kHz of  $\text{SnO}_2/\text{perovskite}$  and APTES-modified  $\text{SnO}_2/\text{perovskite}$  heterojunctions, f) schematic illustration of the band diagram in equilibrium, showing the formation of the  $\text{SnO}_2$  (APTES modified)/perovskite heterojunction. Reproduced with permission.<sup>[159]</sup> Copyright 2016, Royal Society of Chemistry. g) Schematic device structure of the PSCs and the SAM between the  $\text{SnO}_2$  and the perovskite film, h)  $J$ - $V$  curves of the PSCs without and with the different SAMs modifications, and i) ultraviolet photoelectron spectroscopy (UPS) of the  $\text{SnO}_2$  without and with the different SAMs modifications. Reproduced with permission.<sup>[160]</sup> Copyright 2017, American Chemical Society.

the morphology of the perovskite layers dramatically. The SAM modification could increase the surface uniformity and grain size of the perovskite films. When the treatment time was 3 h, the perovskite films exhibited the relatively uniform, smooth surface with favorable grain sizes. The improved morphology of the perovskite films was attributed to the enhanced affinity between the modified  $\text{SnO}_2$  films and the perovskite films. To understand the modification induced impact, the work function (WF) of the  $\text{SnO}_2$  ETLs before and after APTES SAM modification were determined by the Kelvin probe. The WF of the untreated  $\text{SnO}_2$  was 4.75 eV, and the WF value decreased after the modification due to the formation of favorable interface dipoles. Interface dipoles ensured the good energy level matching and efficient electron transport. The long alky chains of the APTES SAM could act as an insulating barrier. The insulating barrier could prevent electron back transfer, reducing recombination and facilitating electron collection. The capacitance–voltage ( $C$ - $V$ ) measurement shown in Figure 8e was used to investigate the properties of the  $\text{SnO}_2/\text{perovskite}$  junction interfaces. As shown in Figure 8f, the ( $\text{SnO}_2 + \text{SAM}$ )/perovskite heterojunction had a high built-in potential ( $V_{bi}$ ), indicating that the decreased WF value of the APTES SAM modified  $\text{SnO}_2$

resulted in the enlarged  $V_{bi}$  and the extended depleted region. The planar  $\text{MAPbI}_3$  solar cells based on  $\text{SnO}_2$  ETL with different APTES treatment times were fabricated. The PSCs based on the  $\text{SnO}_2$  ETL with 3 h APTES treatment showed the best photovoltaic performance with a PCE of 17.03% and the enhanced performance was attributed to the obvious increase of the  $V_{OC}$  value.

Zuo et al. also used the SAM to tune the interfacial optoelectronic properties by bonding the perovskite layers to the  $\text{SnO}_2$ .<sup>[160]</sup> They used different functional group terminated SAM, including benzoic acid (BA), 4-pyridinecarboxylic acid (PA), 3-aminopropanoic acid (C3), 4-aminobenzoic acid (ABA), and 4-cyanobenzoic acid (CBA), to modify the  $\text{SnO}_2$  surfaces and the structure of the solar cells was depicted in Figure 8g. The photovoltaic performance of the solar cells based on the different SAM-modified  $\text{SnO}_2$  is shown in Figure 8h, and the PSCs based on PA-SAM modified  $\text{SnO}_2$  showed the best performance with the best PCE of 18.77%. Except the ABA-SAM and C3-SAM, other group terminated SAM had improved the performance of PSCs compared with the reference samples. The UPS measurement shown in Figure 8i was used to examine the WF of the  $\text{SnO}_2$  with and without the SAM modification. The WF

of the bare  $\text{SnO}_2$  films is  $\approx 4.21$  eV and the WF could be tuned to 4.17 eV, 4.16 eV, 4.29 eV, 4.05 eV, and 4.07 eV after the surface modification with PA, BA, CBA, ABA, and C3, respectively. Therefore, the SAM-modified  $\text{SnO}_2$  substrates were expected to be more suitable as the ETL, following the gradually fitted order of CBA, un-modified, PA, BA, C3, and ABA. However, the PSCs with the different SAM modifications showed the different trend compared to the that of the WF variation. They attributed these abnormal phenomena to the strong chemical interactions between the terminal functional groups of the SAMs and the perovskite layers. Pyridine could have the significant passivation effect at the interfaces of the  $\text{SnO}_2$  and perovskites and lower the WF value of  $\text{SnO}_2$ , so the designed device architecture with the PA modification had the most striking improvement.

### 3.4. Composite $\text{SnO}_2$ with Other Materials

Although  $\text{SnO}_2$  films have shown the better properties as the ETL of PSCs compared with other ETL materials, there are a lot of researches combining  $\text{SnO}_2$  layer with some other metal oxides layer such as  $\text{ZnO}$ ,  $\text{TiO}_2$ , and  $\text{MgO}$ , which can further improve the performance.  $\text{SnO}_2$  has been used as the modification layer for other oxide ETLs to improve the photovoltaic performance as well. These combinations differed from doping other metal elements into  $\text{SnO}_2$  because of the different mechanisms. The doped  $\text{SnO}_2$  were often obtained by incorporating other metal elements into the crystal  $\text{SnO}_2$  and

showed the phase of  $\text{SnO}_2$ . However, the combinations were achieved by combining the two different metal oxides as the ETLs and showed the separated phases. The combination of  $\text{SnO}_2$  and  $\text{TiO}_2$  is the most frequently used combination.

The original purpose of coating  $\text{TiO}_2$  onto  $\text{SnO}_2$  was to increase the compactness of ETL, contributing to reduce recombination, as exhibited in Figure 9a.  $\text{SnO}_2$  films were not as compact as  $\text{TiO}_2$  films when they had the same thickness, leading to a large amount of uncovered TCO. Zhu et al. even used mesoporous  $\text{SnO}_2$  as the ETL of PSCs without the compact layer, resulting in the direct contact between the perovskite film and the cathode.<sup>[125]</sup> PSCs based on the mesoporous  $\text{SnO}_2$  showed the serious recombination and bad photovoltaic performance. Therefore, after preparing the  $\text{SnO}_2$  ETL, the substrates were treated with  $\text{TiCl}_4$  solutions and the  $\text{TiO}_2$  thin films appeared on the  $\text{SnO}_2$  surfaces, followed by fabricating the PSCs. These PSCs had an apparently larger  $V_{\text{OC}}$  and  $J_{\text{SC}}$ , corresponding to a higher PCE, than the PSCs based on the bare  $\text{SnO}_2$  ETL. Electrochemical impedance spectroscopy (EIS) was used to investigate the charge transfer and recombination at the interfaces among  $\text{SnO}_2$ /perovskite/HTL. The Nyquist plots showed that the recombination resistance of PSCs based on  $\text{TiO}_2$ -coated  $\text{SnO}_2$  was much larger than that of PSCs based on the bare  $\text{SnO}_2$ , which was identified that the former had decreased the recombination rate. The upper  $\text{TiO}_2$  could also improve the quality of perovskite films. Rao et al. spin-coated the  $\text{SnO}_2$  nanocolloid sol layer with  $\approx 3$  nm in size synthesized at  $60^{\circ}\text{C}$  onto FTO and then using  $\text{TiCl}_4$  to treat the  $\text{SnO}_2$ .<sup>[161]</sup> The

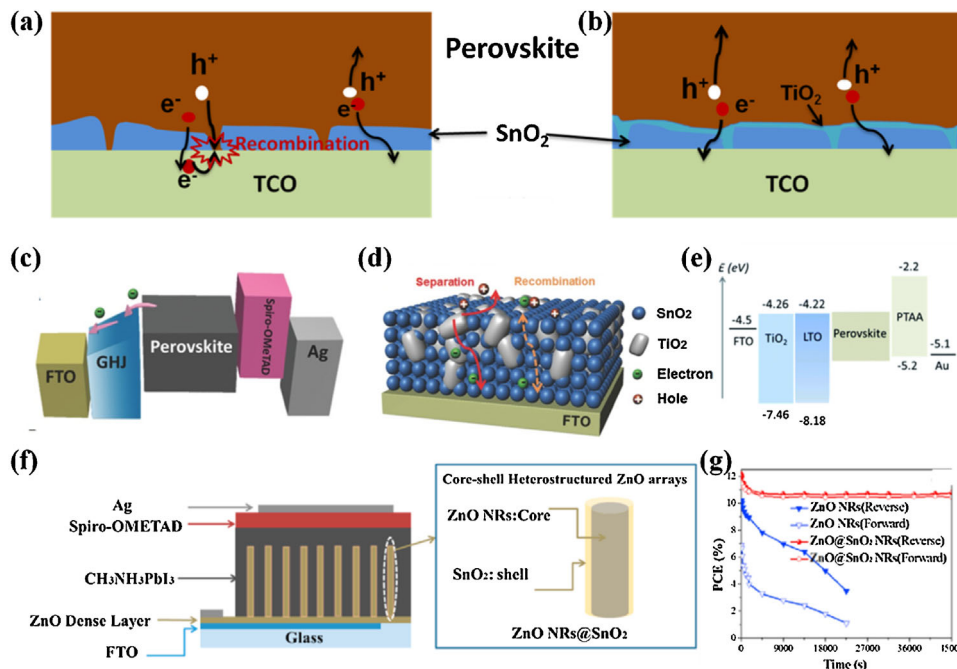


**Figure 9.** a,b) Charge recombination and transfer in the  $\text{SnO}_2$  ( $\text{TiO}_2$  coated  $\text{SnO}_2$ )/perovskite heterojunction. c) Schematic diagram of the potential GHJ ETL-based PSCs, d) schematic illustration of the separation and recombination of photogenerated charges in the devices. Reproduced with permission.<sup>[165]</sup> Copyright 2017, Wiley-VCH. e) Energy band diagram of the  $\text{TiO}_2$ /LTO-based PSCs. Reproduced with permission.<sup>[121]</sup> Copyright 2017, Royal Society of Chemistry. f) Schematic of the device structure based on the core-shell heterostructured  $\text{ZnO}$  arrays (the inset shows the schematic representation of  $\text{SnO}_2$  as the shell structure:  $\text{ZnO}$  nanorods@ $\text{SnO}_2$ ), and g) durability test of PSCs based on the different ETLs under  $100 \text{ mW cm}^{-2}$  AM 1.5G illumination. Reproduced with permission.<sup>[130]</sup> Copyright 2016, Elsevier.

TiCl<sub>4</sub>-treated SnO<sub>2</sub> was used as the ETL of planar PSCs and was demonstrated to contribute to the better crystallization and surface coverage of perovskite films compared with those on the bare SnO<sub>2</sub>. The photovoltaic performance of PSCs based on the TiCl<sub>4</sub>-treated SnO<sub>2</sub> was significantly better than that of non-treated PSCs. The better coverage of the perovskite films reduced recombination, leading to the improved performance.

As demonstrated above, avoiding the contact between perovskite films and TCO can reduce the interface recombination. Thus, Ma et al. incorporated the ultrathin MgO layers prepared by spin-coating between the SnO<sub>2</sub> layers and FTO to reduce the thickness of the SnO<sub>2</sub> films and charge recombination.<sup>[162]</sup> The corresponding energy band diagram is presented in Figure 9b. The MgO films enabled the substrates much smoother compared with the bare FTO. The MgO films filled the gaps between FTO crystals, passivating the FTO surface defects, and made the substrates more uniform, contributing to the better optical transmission and coverage of the SnO<sub>2</sub> films. The MgO layers efficiently blocked charge recombination due to the large energy bandgap of about 7.8 eV. The low valence band position enhanced hole blocking, while the electrons tunneled through the MgO films easily because of the very thin thickness of the MgO. After optimizing the thickness of the MgO films, PSCs with the MgO layer achieved a champion PCE of 18.23% with a  $V_{OC}$  of 1.10 V, a  $J_{SC}$  of 22.7 mA cm<sup>-2</sup>, and a FF of 73%. In contrast, the best-performing PSCs without the MgO had a lower PCE of 16.43% with a  $V_{OC}$  of 1.07 V, a  $J_{SC}$  of 21.63 mA cm<sup>-2</sup>, and a FF of 71%. The higher  $V_{OC}$  and FF were attributed to the reduction of the charge recombination and better charge transfer.

Since the movement of high-mobility electrons in SnO<sub>2</sub> are equally toward both directions, the performance can be further improved via suppressing the electron back-flow. In silicon and organic solar cells, the gradient heterojunction (GHJ) strategy has been widely used to facilitate charge separation due to the potential gradient.<sup>[163,164]</sup> The potential gradient can act as the driving force to promote the electron diffusion toward the desired direction. Due to the lower CB level of SnO<sub>2</sub> than that of TiO<sub>2</sub>, combining these two metal oxides can also define the electron diffusion direction. In ref.<sup>[161]</sup>, the SnO<sub>2</sub> nanocolloid sol layers with TiCl<sub>4</sub> also formed the potential gradient favorable for electron extraction and increasing the coverage of perovskite layers, contributing to improve the performance. However, the architecture of heterojunctions in dual-layered ETLs was planar and the high electron mobility SnO<sub>2</sub> cannot be fully utilized due to the upper compact TiO<sub>2</sub>. Inspired by Wu's work, Hou et al. put forward the GHJ whose energy level structure and architecture is shown in Figure 9c,d, respectively.<sup>[135,165]</sup> They deposited SnO<sub>2</sub> and TiO<sub>2</sub> on FTO glass, respectively, followed by the sintering step. The sintering step led to the mutual infiltration of the adjacent SnO<sub>2</sub> and TiO<sub>2</sub> layers to form the GHJ structure shown in Figure 9d. The GHJ layer was used as ETL of PSCs. The TiO<sub>2</sub> was concentrated at the region closed to the interfaces of GHJ and perovskite layers, and restricted the intense charge recombination due to the potential gradient. Compared with the single TiO<sub>2</sub> ETL-based PSCs, the GHJ ETL-based PSCs exhibited the better photovoltaic performance. The PCE of MAPbI<sub>3</sub> based PSCs was increased from 12.02% to 16.71%, further rising to 18.08% with less hysteresis by replacing MAPbI<sub>3</sub> with Cs<sub>5</sub>(MA<sub>0.17</sub>FA<sub>0.83</sub>)<sub>95</sub>Pb(I<sub>0.83</sub>Br<sub>0.17</sub>)<sub>3</sub>. The PL and

time-resolved PL spectra of the perovskite coated on base FTO, S-TiO<sub>2</sub>, and GHJ ETL were measured. EIS were also used to evaluate the charge transfer in perovskites. All the above characterization results indicated that GHJ ETL not only benefited electron collection and transport, but also reduced the charge recombination.

The former work has also reported that SnO<sub>2</sub> on TiO<sub>2</sub> also can improve the photovoltaic performance of PSCs. TiO<sub>2</sub> is the most commonly used ETL material due to its favorable CB edge, deep valence band position, simple film preparation, and environmental stability are also its great merits. However, TiO<sub>2</sub> has relatively low-electron mobility, leading to insufficient charge separation at the interface between perovskites and TiO<sub>2</sub>. To overcome the this issue, the interface layers were introduced between perovskites and TiO<sub>2</sub>. Acceptor-type organic semiconductor materials such as PCBM and inorganic N-type semiconductor materials with high mobility, such as ZnO and SnO<sub>2</sub>, are commonly used as the interface modification layers. Notably, ZnO has relatively high mobility more than 200 cm<sup>2</sup>V/s, but it has serious stability problems in PSCs and is not suitable for modifying the interfaces. SnO<sub>2</sub> also has relatively high mobility more than 200 cm<sup>2</sup>V/s and has excellent stability. Lee et al. introduced SnO<sub>2</sub> layers by the low-temperature solution process onto the compact TiO<sub>2</sub> layers.<sup>[121]</sup> The SnO<sub>2</sub> was prepared by spin-coating SnCl<sub>4</sub> dissolved in water and followed by annealing. It was found that the passivation effect of SnO<sub>2</sub> depended on the annealing temperature. The low-temperature process confirmed the layer of SnOCl<sub>2</sub> on the surface of SnO<sub>2</sub> and the SnOCl<sub>2</sub> layer acted as the passivation layer (PTO). The low-temperature processed SnO<sub>2</sub> (LTO) also had good energy level alignment and the energy bandgap diagram of PSCs is shown in Figure 9e. However, the high-temperature process accelerated the decomposition of SnOCl<sub>2</sub> to form SnO<sub>2</sub> and increased the defect density on the surfaces of SnO<sub>2</sub>. The high-temperature process also made the CB mismatched between TiO<sub>2</sub> and SnO<sub>2</sub>, resulting in charge recombination and dropped efficiency. To identify the SnO<sub>2</sub>-induced impact on TiO<sub>2</sub>, the performance of PSCs based on the different ETLs was investigated, which clarified that the SnO<sub>2</sub> on TiO<sub>2</sub> had improved the photovoltaic performance dramatically. Ding et al. also used SnO<sub>2</sub> to treat TiO<sub>2</sub> films.<sup>[103]</sup> The preparation process of ETL was described as following. To gain the compact TiO<sub>2</sub> films, they soaked the substrates into high-concentration TiCl<sub>4</sub> solution and then soaked the substrate into low-concentration TiCl<sub>4</sub> to densify the films obtained in the previous step. After preparing TiO<sub>2</sub>, the samples were immersed into SnCl<sub>2</sub> solution. The temperature of the chemical bath was 70 °C in the above three steps. Finally, the samples were annealed at 140 °C and the SnO<sub>2</sub>-modified TiO<sub>2</sub> films (SnO<sub>2</sub>@TiO<sub>2</sub>) were prepared. The PSCs based on TiO<sub>2</sub> and SnO<sub>2</sub>@TiO<sub>2</sub> were, respectively, fabricated. The  $J-V$  curves of PSCs based on TiO<sub>2</sub> and SnO<sub>2</sub>@TiO<sub>2</sub> were measured under the illumination to identify the photovoltaic performance, showing that the PSCs based on SnO<sub>2</sub>@TiO<sub>2</sub> had reduced hysteresis. Compared with the devices using TiO<sub>2</sub> as ETLs, the devices using SnO<sub>2</sub>@TiO<sub>2</sub> as ETLs exhibited better photovoltaic performance, the corresponding mechanism of which was the same as explained in ref.<sup>[121]</sup> In this work, the PCE of planar PSCs based on SnO<sub>2</sub>@TiO<sub>2</sub> stabilized at 21.56% that is one of the highest reported PCE for planar PSCs up to now.

ZnO is another promising material for ETL of PSCs due to its low-temperature process and high electron mobility, and was widely studied as the ETL of PSCs by researchers especially before achieving the high-performance PSCs based on SnO<sub>2</sub> ETLs. However, PSCs based on ZnO suffered from serious instability. Many hydroxides ( $-OH$ ) were on ZnO surfaces and can break the ionic interaction between  $CH_3NH_3^+$  and PbI<sub>3</sub><sup>-</sup>.<sup>[166]</sup> Avoiding or reducing the contact between the perovskites and hydroxides is an effective method to improve the stability of PSCs. Some work has reported that using ultrathin oxides or self-assembled molecular layers can modify the surfaces, and thus improve the photovoltaic performance and stability.<sup>[79,130,167–168]</sup> Wang et al. used the electrochemical method to grow ZnO nanorods on ZnO dense layers as the ETL of PSCs.<sup>[130]</sup> Then they spin-coated SnCl<sub>2</sub> solution on the ZnO nanorods and then sintered samples to form a SnO<sub>2</sub> thin films on surfaces of ZnO nanorods. The hydroxyl groups might be trapped in oxygen vacancies on SnO<sub>2</sub> films. The blocking layer inhibited the contract between ZnO nanorods and perovskite films, avoiding the perovskite decomposition. The structure diagram of devices is shown in Figure 9f. Therefore, coating ZnO nanorods with SnO<sub>2</sub> can enhance the stability of perovskites on ETL when heated in air and improved the photovoltaic performance. The long-term stability as a function of time was characterized and the results are shown in Figure 9g. The PCE of the PSCs based on ZnO@SnO<sub>2</sub> nanorods remained stable within 45 000 s, though there was a slight drop in the beginning. In contrast, the power output of the PSCs based on the bare ZnO nanorods showed sustaining decrease. The obvious difference in long-term stability suggested that the SnO<sub>2</sub> layer acted as a role of passivation layer to stabilize the PSCs.

Besides coating SnO<sub>2</sub> on ZnO surfaces, using ZnO–SnO<sub>2</sub> nanocomposites can also enhance the stability of PSCs. Song et al. mixed ZnO nanoparticles with SnO<sub>2</sub> nanoparticles to prepare ZnO–SnO<sub>2</sub> composites as the ETLs for PSCs, and then using two-step sequential deposition technique to grow the MAPbI<sub>3</sub> perovskite films.<sup>[169]</sup> They found that the planar PSCs exhibited improved performance with the optimal weight ratio of 2:1 for ZnO/SnO<sub>2</sub>. ZnO had higher mobility of  $5.9 \times 10^{-3} \text{ cm}^2 \text{ V}^{-1} \text{ s}^{-1}$  compared with SnO<sub>2</sub> with mobility of  $2.2 \times 10^{-3} \text{ cm}^2 \text{ V}^{-1} \text{ s}^{-1}$ , leading to relatively higher electrical conductivity in ZnO films. In addition, SnO<sub>2</sub> had the deeper CB edge compared with ZnO, resulting in better electron extraction. Therefore, the ZnO–SnO<sub>2</sub> composites inherited both advantages to improve the photovoltaic performance. The thermal stability of MAPbI<sub>3</sub> on the different ETLs was investigated. The perovskite films on the bare ZnO showed the worst thermal stability among these samples. In comparison, the perovskite films on ZnO–SnO<sub>2</sub> showed relatively better thermal stability. The stability result of the PSCs based on ZnO, ZnO–SnO<sub>2</sub> (2:1) and SnO<sub>2</sub> as ETLs during the storage in ambient conditions at room temperature was consistent with the thermal stability results of MAPbI<sub>3</sub> on the different ETLs. The thermal stability of PSCs was due to the reduced hydroxyl residues.

Compositing SnO<sub>2</sub> with some organic materials can also enhance the photovoltaic performance. Yang et al. mixed SnO<sub>2</sub> nanoparticles dispersed solution with ethylene diamine tetra-acetic acid (EDTA) to form EDTA-complexed SnO<sub>2</sub> (E-SnO<sub>2</sub>).<sup>[170]</sup> Compared with pristine SnO<sub>2</sub> and EDTA films, E-SnO<sub>2</sub> film

showed a lower WF and much better energy match with perovskite. The electron mobility of ETL also improved dramatically. The crystallization of perovskite film (Cs<sub>0.05</sub>FA<sub>0.95</sub>PbI<sub>3</sub>) on E-SnO<sub>2</sub> also was improved dramatically, leading to less bulk defects in perovskite film. Hence, PSCs based on E-SnO<sub>2</sub> showed a perfect photovoltaic performance yielding a PCE of 21.60%. This is the highest reported PCE based on SnO<sub>2</sub> up to now.

#### 4. Summary and Outlook

PSCs have attracted extensive attention, owing to their rapid-PCE development and remarkable low-cost fabrication. The fast progress was attributed to the improvement of each layer, including ETL, light-harvester layer, and HTL. Due to its proper bandgap, deep CB edge, good light transmission, and high electron mobility, SnO<sub>2</sub> is one of the most promising ETLs for PSCs, and the SnO<sub>2</sub>-based PSCs have been developed rapidly since it was used as the ETL material for PSCs for the first time in 2015.

SnO<sub>2</sub>-based PSCs possess different device structures, including planar, mesoporous, inverted and flexible substrate-based structures. Various deposition methods for SnO<sub>2</sub> to suit different structures have been developed, which can be categorized into two major methods. One is based on solution process and another is vapor deposition. The solution based method mainly contains two steps. Preparing the precursor solution is the first step and then depositing SnO<sub>2</sub> films onto substrates through spin-coating or CBD followed by annealing. Although the annealing temperature of conventional solution method is much lower than that of TiO<sub>2</sub> preparation, it is still too high for flexible PSCs or inverted structure PSCs. Thus, lots of work has been carried out to lower the process temperature, such as introducing dispersed SnO<sub>2</sub> nanoparticles as the precursor. The solution based methods are low-cost and have the simple process. However, they were involved with the spin-coating step and were incompatible with large-area fabrication of PSCs. On the other hand, the vapor deposition methods, including physical vapor deposition and chemical vapor deposition, have been used to deposit SnO<sub>2</sub>. In chemical vapor deposition, the ozone and oxygen plasma with strong oxidability were often used as the oxygen source to lower the deposition temperature.

Like other metal oxidation, pristine SnO<sub>2</sub> films contain a lot of bulk and surface defects after prepared, which would capture electrons and deteriorate the electronic properties. To improve the electrical properties, doping SnO<sub>2</sub> and modifying the surfaces of SnO<sub>2</sub> to have been widely studied. Doping bulk SnO<sub>2</sub> with some specific metal elements, such as Nb and Sb, can passivate defects. These metal elements provide excess electrons and the excess can fill the defects, resulting in higher Fermi energy level. Modifying SnO<sub>2</sub> with fullerene and other materials like 4-pyridinecarboxylic acid can passivate the interface defects between perovskite films and SnO<sub>2</sub> films, and enhance the WF of ETL. The passivated SnO<sub>2</sub> shows better electronic properties and improves the photovoltaic performance of PSCs. However, not all metal elements doped in SnO<sub>2</sub> can be used to passivate defects. Some metal elements doped in SnO<sub>2</sub>, like Mg and Y, are used to improve the morphology of ETL.

Using  $\text{SnO}_2$  as the modified material of other metal oxide ETLs or combining  $\text{SnO}_2$  with other metal oxides is another important research. The initial purpose of combining different metal oxides was to improve the ETL morphology. Then the combination was developed to form GHJs and facilitate the charge separation.  $\text{SnO}_2$  was used as the modified material of other ETLs such as  $\text{ZnO}$  and  $\text{TiO}_2$  by some research groups. The low-temperature solution based  $\text{SnO}_2$  films often contained many Cl atoms on the surfaces, which can act as the passivation layer between perovskites and ETLs, and they had excellent energy level match at the interfaces of  $\text{ZnO}$ /perovskites or  $\text{TiO}_2$ /perovskites. The stabilized PCE of PSCs based on  $\text{SnO}_2$  modified  $\text{TiO}_2$  has reached to 21.56% that is the highest reported PCE for planar PSCs up to now. PSCs based on  $\text{SnO}_2$  modified  $\text{ZnO}$  showed both enhanced photovoltaic performance and improved stability.

Although the history of employing  $\text{SnO}_2$  as the ETLs is much shorter than  $\text{TiO}_2$ , the PSCs based on  $\text{SnO}_2$  developed rapidly and the highest reported PCE is comparable with the recorded PCE due to many merits in electron transport. Since the high-performance large-area PSCs and solar modules have been prepared, the large-scale fabrication of PSCs is not the main issue blocking the commercialization of PSCs any more.<sup>[7,171-173]</sup> More and more attention will be paid to the stability of PSCs and further lowering the fabrication cost. To fully take advantages of PSCs, flexibility of PSCs is an important tendency for the commercialization. The  $\text{SnO}_2$ -based PSCs not only show much more stable and excellent performance compared with  $\text{TiO}_2$ -based PSCs, but also can be prepared by the low-temperature process. Therefore,  $\text{SnO}_2$  is one of the most promising substitutes of  $\text{TiO}_2$  and the  $\text{SnO}_2$ -based PSCs have better performance and stability with more devoted effort.

## Acknowledgements

This work was supported by National Natural Science Foundation of China under Grant Nos. 61421002, 61874150, 61574029, and 61471085. This work was also partially supported by University of Kentucky. The manuscript was written through contributions of all authors. All authors have given approval to the final version of the manuscript.

## Conflict of Interest

The authors declare no competing financial interests.

## Keywords

configuration design, performance improvement, perovskite solar cells, tin dioxide

Received: October 15, 2018

Revised: November 15, 2018

Published online:

[1] F. Di Giacomo, A. Fakharuddin, R. Jose, T. M. Brown, *Energy Environ. Sci.* **2016**, *9*, 3007.

- [2] Z. Shi, J. Guo, Y. Chen, Q. Li, Y. Pan, H. Zhang, Y. Xia, W. Huang, *Adv. Mater.* **2017**, *29*, 1605005.
- [3] W. S. Yang, B. W. Park, E. H. Jung, N. J. Jeon, Y. C. Kim, D. U. Lee, S. S. Shin, J. Seo, E. K. Kim, J. H. Noh, S. I. Seok, *Science* **2017**, *356*, 1376.
- [4] S. S. Shin, E. J. Yeom, W. S. Yang, S. Hur, M. G. Kim, J. Im, J. Seo, J. H. Noh, S. I. Seok, *Science* **2017**, *356*, 167.
- [5] Y. Hou, X. Du, S. Scheiner, D. P. McMeekin, Z. Wang, N. Li, M. S. Killian, H. Chen, M. Richter, I. Levchuk, N. Schrenker, E. Spiecker, T. Stubhan, N. A. Luechinger, A. Hirsch, P. Schmuki, H. P. Steinrück, R. H. Fink, M. Halik, H. J. Snaith, C. J. Brabec, *Science* **2017**, *358*, 1192.
- [6] N. Arora, M. I. Dar, A. Hinderhofer, N. Pellet, F. Schreiber, S. M. Zakeeruddin, M. Gratzel, *Science* **2017**, *358*, 768.
- [7] H. Chen, F. Ye, W. Tang, J. He, M. Yin, Y. Wang, F. Xie, E. Bi, X. Yang, M. Gratzel, L. Han, *Nature* **2017**, *550*, 92.
- [8] M. A. Green, A. Ho-Baillie, H. J. Snaith, *Nat. Photon.* **2014**, *8*, 506.
- [9] R. J. Sutton, G. E. Eperon, L. Miranda, E. S. Parrott, B. A. Kamino, J. B. Patel, M. T. Horantner, M. B. Johnston, A. A. Haghighirad, D. T. Moore, H. J. Snaith, *Adv. Energy Mater.* **2016**, *6*, 1502458.
- [10] M. Deepa, M. Salado, L. Calio, S. Kazim, S. M. Shivaprasad, S. Ahmad, *Phys. Chem. Chem. Phys.* **2017**, *19*, 4069.
- [11] M. Saliba, T. Matsui, J.-Y. Seo, K. Domanski, J.-P. Correa-Baena, M. K. Nazeeruddin, S. M. Zakeeruddin, W. Tress, A. Abate, A. Hagfeldt, M. Grätzel, *Energy Environ. Sci.* **2016**, *9*, 1989.
- [12] C. Yi, J. Luo, S. Meloni, A. Boziki, N. Ashari-Astani, C. Grätzel, S. M. Zakeeruddin, U. Röthlisberger, M. Grätzel, *Energy Environ. Sci.* **2016**, *9*, 656.
- [13] J.-W. Lee, D.-H. Kim, H.-S. Kim, S.-W. Seo, S. M. Cho, N.-G. Park, *Adv. Energy Mater.* **2015**, *5*, 1501310.
- [14] J.-P. Correa-Baena, E. Halvani Anaraki, A. Kermanpur, L. Steier, K. Domanski, T. Matsui, W. Tress, M. Saliba, A. Abate, M. Grätzel, A. Hagfeldt, *Energy Environ. Sci.* **2016**, *9*, 3128.
- [15] M. Kulbak, D. Cahen, G. Hodes, *J. Phys. Chem. Lett.* **2015**, *6*, 2452.
- [16] D. P. McMeekin, G. Sadoughi, W. Rehman, G. E. Eperon, M. Saliba, M. T. Horantner, A. Haghighirad, N. Sakai, L. Korte, B. Rech, M. B. Johnston, L. M. Herz, H. J. Snaith, *Science* **2016**, *351*, 151.
- [17] J. K. Nam, S. U. Chai, W. Cha, Y. J. Choi, W. Kim, M. S. Jung, J. Kwon, D. Kim, J. H. Park, *Nano Lett.* **2017**, *17*, 2028.
- [18] Y. Hassan, Y. Song, R. D. Pensack, A. I. Abdelrahman, Y. Kobayashi, M. A. Winnik, G. D. Scholes, *Adv. Mater.* **2016**, *28*, 566.
- [19] Y. Wang, J. Wu, P. Zhang, D. Liu, T. Zhang, L. Ji, X. Gu, Z. David Chen, S. Li, *Nano Energy* **2017**, *39*, 616.
- [20] M. Saliba, T. Matsui, K. Domanski, J. Y. Seo, A. Ummadisingu, S. M. Zakeeruddin, J. P. Correa-Baena, W. R. Tress, A. Abate, A. Hagfeldt, M. Grätzel, *Science* **2016**, *354*, 206.
- [21] N. J. Jeon, J. H. Noh, W. S. Yang, Y. C. Kim, S. Ryu, J. Seo, S. I. Seok, *Nature* **2015**, *517*, 476.
- [22] W. S. Yang, J. H. Noh, N. J. Jeon, Y. C. Kim, S. Ryu, J. Seo, S. I. Seok, *Science* **2015**, *348*, 1234.
- [23] R. Zhang, D. Liu, Y. Wang, T. Zhang, X. Gu, P. Zhang, J. Wu, Z. D. Chen, Y. Zhao, S. Li, *Electrochim. Acta* **2018**, *265*, 98.
- [24] F. Hao, C. C. Stoumpos, D. H. Cao, R. P. H. Chang, M. G. Kanatzidis, *Nat. Photon.* **2014**, *8*, 489.
- [25] Z. Yang, A. Rajagopal, C. C. Chueh, S. B. Jo, B. Liu, T. Zhao, A. K. Jen, *Adv. Mater.* **2016**, *28*, 8990.
- [26] B. Zhao, M. Abdi-Jalebi, M. Tabachnyk, H. Glass, V. S. Kamboj, W. Nie, A. J. Pearson, Y. Puttisong, K. C. Godel, H. E. Beere, D. A. Ritchie, A. D. Mohite, S. E. Dutton, R. H. Friend, A. Sadhanala, *Adv. Mater.* **2017**, *29*, 1604744.
- [27] N. K. Noel, S. D. Stranks, A. Abate, C. Wehrenfennig, S. Guarnera, A. A. Haghighirad, A. Sadhanala, G. E. Eperon, S. K. Pathak,

- M. B. Johnston, A. Petrozza, L. M. Herz, H. J. Snaith, *Energy Environ. Sci.* **2014**, *7*, 3061.
- [28] Y. Ogomi, A. Morita, S. Tsukamoto, T. Saitho, N. Fujikawa, Q. Shen, T. Toyoda, K. Yoshino, S. S. Pandey, T. Ma, S. Hayase, *J. Phys. Chem. Lett.* **2014**, *5*, 1004.
- [29] F. Hao, C. C. Stoumpos, R. P. Chang, M. G. Kanatzidis, *J. Am. Chem. Soc.* **2014**, *136*, 8094.
- [30] P. P. Boix, K. Nonomura, N. Mathews, S. G. Mhaisalkar, *Mater. Today* **2014**, *17*, 16.
- [31] H. S. Jung, N. G. Park, *Small* **2015**, *11*, 10.
- [32] H. J. Snaith, *J. Phys. Chem. Lett.* **2013**, *4*, 3623.
- [33] N. Pellet, P. Gao, G. Gregori, T. Y. Yang, M. K. Nazeeruddin, J. Maier, M. Grätzel, *Angew. Chem.* **2014**, *53*, 3151.
- [34] J. H. Noh, S. H. Im, J. H. Heo, T. N. Mandal, S. I. Seok, *Nano Lett.* **2013**, *13*, 1764.
- [35] S. D. Stranks, G. E. Eperon, G. Grancini, C. Menelaou, M. J. Alcocer, T. Leijtens, L. M. Herz, A. Petrozza, H. J. Snaith, *Science* **2013**, *342*, 341.
- [36] A. Kojima, K. Teshima, T. Miyasaka, Y. Shirai, A. Kojima, K. Teshima, T. Miyasaka, Y. Shirai, *210th ECS Meeting, Cancun (October, 2006)*.
- [37] A. Kojima, K. Teshima, Y. Shirai, T. Miyasaka, *J. Am. Chem. Soc.* **2009**, *131*, 6050.
- [38] J. H. Im, C. R. Lee, J. W. Lee, S. W. Park, N. G. Park, *Nanoscale* **2011**, *3*, 4088.
- [39] H. S. Kim, C. R. Lee, J. H. Im, K. B. Lee, T. Moehl, A. Marchioro, S. J. Moon, R. Humphry-Baker, J. H. Yum, J. E. Moser, M. Grätzel, N. G. Park, *Sci. Rep.* **2012**, *2*, 591.
- [40] J. Burschka, N. Pellet, S. J. Moon, R. Humphry-Baker, P. Gao, M. K. Nazeeruddin, M. Grätzel, *Nature* **2013**, *499*, 316.
- [41] H. Zhou, Q. Chen, G. Li, S. Luo, T. B. Song, H. S. Duan, Z. Hong, J. You, Y. Liu, Y. Yang, *Science* **2014**, *345*, 542.
- [42] G. E. Eperon, S. D. Stranks, C. Menelaou, M. B. Johnston, L. M. Herz, H. J. Snaith, *Energy Environ. Sci.* **2014**, *7*, 982.
- [43] T. M. Koh, K. Fu, Y. Fang, S. Chen, T. C. Sum, N. Mathews, S. G. Mhaisalkar, P. P. Boix, T. Baikie, *J. Phys. Chem. C* **2014**, *118*, 16458.
- [44] J. W. Lee, D. J. Seol, A. N. Cho, N. G. Park, *Adv. Mater.* **2014**, *26*, 4991.
- [45] S. Pang, H. Hu, J. Zhang, S. Lv, Y. Yu, F. Wei, T. Qin, H. Xu, Z. Liu, G. Cui, *Chem. Mater.* **2014**, *26*, 1485.
- [46] National Renewable Energy Laboratory, Best Research-Cell Efficiencies, <https://www.nrel.gov/pv/assets/images/efficiency-chart-20180716.jpg> (accessed: July, 2018).
- [47] D. Liu, Y. Wang, H. Zheng, J. Wu, L. Ji, P. Zhang, W. Ahmad, H. Chen, Z. Chen, S. Li, *Electrochim. Acta* **2019**, *296*, 508.
- [48] S. D. Stranks, H. J. Snaith, *Nat. Nanotechnol.* **2015**, *10*, 391.
- [49] Y. Wang, S. Li, P. Zhang, D. Liu, X. Gu, H. Sarvari, Z. Ye, J. Wu, Z. Wang, Z. D. Chen, *Nanoscale* **2016**, *8*, 19654.
- [50] W. Ke, G. Fang, Q. Liu, L. Xiong, P. Qin, H. Tao, J. Wang, H. Lei, B. Li, J. Wan, G. Yang, Y. Yan, *J. Am. Chem. Soc.* **2015**, *137*, 6730.
- [51] J. P. Correa Baena, L. Steier, W. Tress, M. Saliba, S. Neutzner, T. Matsui, F. Giordano, T. J. Jacobsson, A. R. Srimath Kandada, S. M. Zakeeruddin, A. Petrozza, A. Abate, M. K. Nazeeruddin, M. Grätzel, A. Hagfeldt, *Energy Environ. Sci.* **2015**, *8*, 2928.
- [52] J. You, L. Meng, T. B. Song, T. F. Guo, Y. M. Yang, W. H. Chang, Z. Hong, H. Chen, H. Zhou, Q. Chen, Y. Liu, N. De Marco, Y. Yang, *Nat. Nanotechnol.* **2016**, *11*, 75.
- [53] E. J. Crossland, N. Noel, V. Sivaram, T. Leijtens, J. A. Alexander-Webber, H. J. Snaith, *Nature* **2013**, *495*, 215.
- [54] Y. Shao, Y. Yuan, J. Huang, *Nat. Energy* **2016**, *1*, 15001.
- [55] X. Yin, Z. Yao, Q. Luo, X. Dai, Y. Zhou, Y. Zhang, Y. Zhou, S. Luo, J. Li, N. Wang, H. Lin, *ACS Appl. Mater. Interfaces* **2017**, *9*, 2439.
- [56] C.-H. Chiang, Z.-L. Tseng, C.-G. Wu, *J. Mater. Chem. A* **2014**, *2*, 15897.
- [57] P.-W. Liang, C.-C. Chueh, S. T. Williams, A. K. Y. Jen, *Adv. Energy Mater.* **2015**, *5*, n/a.
- [58] H. Yoon, S. M. Kang, J.-K. Lee, M. Choi, *Energy Environ. Sci.* **2016**, *9*, 2262.
- [59] D. Yang, R. Yang, X. Ren, X. Zhu, Z. Yang, C. Li, S. F. Liu, *Adv. Mater.* **2016**, *28*, 5206.
- [60] S. S. Shin, W. S. Yang, J. H. Noh, J. H. Suk, N. J. Jeon, J. H. Park, J. S. Kim, W. M. Seong, S. I. Seok, *Nat. Commun.* **2015**, *6*, 7410.
- [61] K. Wang, Y. Shi, Q. Dong, Y. Li, S. Wang, X. Yu, M. Wu, T. Ma, J. *Phys. Chem. Lett.* **2015**, *6*, 755.
- [62] C. Tao, S. Neutzner, L. Colella, S. Marras, A. R. Srimath Kandada, M. Gandini, M. D. Bastiani, G. Pace, L. Manna, M. Caireoni, C. Bertarelli, A. Petrozza, *Energy Environ. Sci.* **2015**, *8*, 2365.
- [63] Y. Zhao, H. Zhang, X. Ren, H. L. Zhu, Z. Huang, F. Ye, D. Ouyang, K. W. Cheah, A. K. Y. Jen, W. C. H. Choy, *ACS Energy Letters* **2018**, *3*, 2891.
- [64] W. Ke, G. Fang, J. Wang, P. Qin, H. Tao, H. Lei, Q. Liu, X. Dai, X. Zhao, *ACS Appl. Mater. Interfaces* **2014**, *6*, 15959.
- [65] A. Agresti, S. Pescetelli, L. Cinà, D. Konios, G. Kakavelakis, E. Kymakis, A. D. Carlo, *Adv. Funct. Mater.* **2016**, *26*, 2686.
- [66] S. Hong, A. Han, E. C. Lee, K.-W. Ko, J.-H. Park, H.-J. Song, M.-H. Han, C.-H. Han, *Curr. Appl. Phys.* **2015**, *15*, 574.
- [67] N. J. Jeon, J. H. Noh, Y. C. Kim, W. S. Yang, S. Ryu, S. I. Seok, *Nat. Mater.* **2014**, *13*, 897.
- [68] J. H. Heo, H. J. Han, D. Kim, T. K. Ahn, S. H. Im, *Energy Environ. Sci.* **2015**, *8*, 1602.
- [69] P. Qin, M. Paulose, M. I. Dar, T. Moehl, N. Arora, P. Gao, O. K. Varghese, M. Grätzel, M. K. Nazeeruddin, *Small* **2015**, *11*, 5533.
- [70] F. Giordano, A. Abate, J. P. Correa Baena, M. Saliba, T. Matsui, S. H. Im, S. M. Zakeeruddin, M. K. Nazeeruddin, A. Hagfeldt, M. Graetzel, *Nat. Commun.* **2016**, *7*, 10379.
- [71] F. Di Giacomo, V. Zardetto, A. D'Epifanio, S. Pescetelli, F. Matteocci, S. Razza, A. Di Carlo, S. Licoccia, W. M. M. Kessels, M. Creatore, T. M. Brown, *Adv. Energy Mater.* **2015**, *5*, 1614.
- [72] Y. Wu, X. Yang, H. Chen, K. Zhang, C. Qin, J. Liu, W. Peng, A. Islam, E. Bi, F. Ye, M. Yin, P. Zhang, L. Han, *Appl. Phys. Express* **2014**, *7*, 052301.
- [73] D. Liu, S. Li, P. Zhang, Y. Wang, R. Zhang, H. Sarvari, F. Wang, J. Wu, Z. Wang, Z. D. Chen, *Nano Energy* **2017**, *31*, 462.
- [74] X. Gu, Y. Wang, T. Zhang, D. Liu, R. Zhang, P. Zhang, J. Wu, Z. D. Chen, S. Li, *J. Mater. Chem. C* **2017**, *5*, 10754.
- [75] P. Zhang, J. Wu, T. Zhang, Y. Wang, D. Liu, H. Chen, L. Ji, C. Liu, W. Ahmad, Z. D. Chen, S. Li, *Adv. Mater.* **2018**, *30*, 1703737.
- [76] D. Liu, T. L. Kelly, *Nat. Photon.* **2013**, *8*, 133.
- [77] L.-L. Gao, L.-S. Liang, X.-X. Song, B. Ding, G.-J. Yang, B. Fan, C.-X. Li, C.-J. Li, *J. Mater. Chem. A* **2016**, *4*, 3704.
- [78] J. H. Heo, M. H. Lee, H. J. Han, B. R. Patil, J. S. Yu, S. H. Im, *J. Mater. Chem. A* **2016**, *4*, 1572.
- [79] J. Cao, B. Wu, R. Chen, Y. Wu, Y. Hui, B. W. Mao, N. Zheng, *Adv. Mater.* **2018**, *30*, 1705596.
- [80] P. Zhang, J. Wu, Y. Wang, H. Sarvari, D. Liu, Z. D. Chen, S. Li, *J. Mater. Chem. A* **2017**, *5*, 17368.
- [81] D. Liu, Y. Wang, Z. She, H. Zheng, P. Zhang, F. Wang, J. Wu, Z. Chen, S. Li, *Sol. RRL* **2018**, *2*, 1800240.
- [82] M. A. Mahmud, N. K. Elumalai, M. B. Upama, D. Wang, V. R. Gonçales, M. Wright, C. Xu, F. Haque, A. Uddin, *J. Power Sources* **2018**, *383*, 59.
- [83] R. Fang, S. Wu, W. Chen, Z. Liu, S. Zhang, R. Chen, Y. Yue, L. Deng, Y. B. Cheng, L. Han, W. Chen, *ACS Nano* **2018**, *12*, 2403.

- [84] A. Kogo, Y. Numata, M. Ikegami, T. Miyasaka, *Chem. Lett.* **2015**, 44, 829.
- [85] J. Feng, Z. Yang, D. Yang, X. Ren, X. Zhu, Z. Jin, W. Zi, Q. Wei, S. Liu, *Nano Energy* **2017**, 36, 1.
- [86] J.-I. Park, J. H. Heo, S.-H. Park, K. I. Hong, H. G. Jeong, S. H. Im, H.-K. Kim, *J. Power Sources* **2017**, 341, 340.
- [87] S. S. Shin, W. S. Yang, E. J. Yeom, S. J. Lee, N. J. Jeon, Y. C. Joo, I. J. Park, J. H. Noh, S. I. Seok, *J. Phys. Chem. Lett.* **2016**, 7, 1845.
- [88] X. Liu, C.-C. Chueh, Z. Zhu, S. B. Jo, Y. Sun, A. K. Y. Jen, *J. Mater. Chem. A* **2016**, 4, 15294.
- [89] J. H. Park, J. Seo, S. Park, S. S. Shin, Y. C. Kim, N. J. Jeon, H. W. Shin, T. K. Ahn, J. H. Noh, S. C. Yoon, C. S. Hwang, S. I. Seok, *Adv. Mater.* **2015**, 27, 4013.
- [90] J. Seo, S. Park, Y. Chan Kim, N. J. Jeon, J. H. Noh, S. C. Yoon, S. I. Seok, *Energy Environ. Sci.* **2014**, 7, 2642.
- [91] Y. Shao, Z. Xiao, C. Bi, Y. Yuan, J. Huang, *Nat. Commun.* **2014**, 5, 5784.
- [92] Y. Deng, Q. Dong, C. Bi, Y. Yuan, J. Huang, *Adv. Energy Mater.* **2016**, 6, 1600372.
- [93] J. Pascual, J. L. Delgado, R. Tena-Zaera, *J. Phys. Chem. Lett.* **2018**, 9, 2893.
- [94] J. Pascual, I. Kosta, T. Tuyen Ngo, A. Chuvinilin, G. Cabanero, H. J. Grande, E. M. Barea, I. Mora-Sero, J. L. Delgado, R. Tena-Zaera, *ChemSusChem* **2016**, 9, 2679.
- [95] S. Collavini, M. Saliba, W. R. Tress, P. J. Holzhey, S. F. Volker, K. Domanski, S. H. Turren-Cruz, A. Ummadisingu, S. M. Zakeeruddin, A. Hagfeldt, M. Gratzel, J. L. Delgado, *ChemSusChem* **2018**, 11, 1032.
- [96] M. Park, J.-Y. Kim, H. J. Son, C.-H. Lee, S. S. Jang, M. J. Ko, *Nano Energy* **2016**, 26, 208.
- [97] W. Ke, D. Zhao, A. J. Cimaroli, C. R. Grice, P. Qin, Q. Liu, L. Xiong, Y. Yan, G. Fang, *J. Mater. Chem. A* **2015**, 3, 24163.
- [98] J. P. Cheng, J. Wang, Q. Q. Li, H. G. Liu, Y. Li, *J. Ind. Eng. Chem.* **2016**, 44, 1.
- [99] B. Roose, J.-P. C. Baena, K. C. Gödel, M. Graetzel, A. Hagfeldt, U. Steiner, A. Abate, *Nano Energy* **2016**, 30, 517.
- [100] X. Ren, D. Yang, Z. Yang, J. Feng, X. Zhu, J. Niu, Y. Liu, W. Zhao, S. F. Liu, *ACS Appl. Mater. Interfaces* **2017**, 9, 2421.
- [101] J. Barbe, M. L. Tietze, M. Neophytou, B. Murali, E. Alarousu, A. El Labban, M. Abulikemu, W. Yue, O. F. Mohammed, I. McCulloch, A. Amassian, S. Del Gobbo, *ACS Appl. Mater. Interfaces* **2017**, 9, 11828.
- [102] Q. Jiang, Z. Chu, P. Wang, X. Yang, H. Liu, Y. Wang, Z. Yin, J. Wu, X. Zhang, J. You, *Adv. Mater.* **2017**, 29, 1703852.
- [103] B. Ding, S.-Y. Huang, Q.-Q. Chu, Y. Li, C.-X. Li, C.-J. Li, G.-J. Yang, *J. Mater. Chem. A* **2018**, 6, 10233.
- [104] D. Yang, R. Yang, K. Wang, C. Wu, X. Zhu, J. Feng, X. Ren, G. Fang, S. Priya, S. F. Liu, *Nat. Commun.* **2018**, 9, 3239.
- [105] M. Grätzel, *J. Photochem. Photobiol. C* **2003**, 4, 145.
- [106] X. Wang, Z. Li, W. Xu, S. A. Kulkarni, S. K. Batabyal, S. Zhang, A. Cao, L. H. Wong, *Nano Energy* **2015**, 11, 728.
- [107] M. H. Kumar, N. Yantara, S. Dharani, M. Graetzel, S. Mhaisalkar, P. P. Boix, N. Mathews, *Chem. Commun.* **2013**, 49, 11089.
- [108] H. Tao, W. Ke, J. Wang, Q. Liu, J. Wan, G. Yang, G. Fang, *J. Power Sources* **2015**, 290, 144.
- [109] M. M. Lee, J. Teuscher, T. Miyasaka, T. N. Murakami, H. J. Snaith, *Science* **2012**, 338, 643.
- [110] K.-H. Jung, J.-Y. Seo, S. Lee, H. Shin, N.-G. Park, *J. Mater. Chem. A* **2017**, 5, 24790.
- [111] X. Liu, K.-W. Tsai, Z. Zhu, Y. Sun, C.-C. Chueh, A. K. Y. Jen, *Adv. Mater. Interfaces* **2016**, 3, 1600122.
- [112] J. Song, E. Zheng, J. Bian, X.-F. Wang, W. Tian, Y. Sanehira, T. Miyasaka, *J. Mater. Chem. A* **2015**, 3, 10837.
- [113] Q. Jiang, L. Zhang, H. Wang, X. Yang, J. Meng, H. Liu, Z. Yin, J. Wu, X. Zhang, J. You, *Nat. Energy* **2016**, 1, 16177.
- [114] M. Abulikemu, M. Neophytou, J. M. Barbé, M. L. Tietze, A. El Labban, D. H. Anjum, A. Amassian, I. McCulloch, S. Del Gobbo, *J. Mater. Chem. A* **2017**, 5, 7759.
- [115] J. Ba, J. Polleux, M. Antonietti, M. Niederberger, *Adv. Mater.* **2005**, 17, 2509.
- [116] G. Yang, C. Chen, F. Yao, Z. Chen, Q. Zhang, X. Zheng, J. Ma, H. Lei, P. Qin, L. Xiong, W. Ke, G. Li, Y. Yan, G. Fang, *Adv. Mater.* **2018**, 30, 1706023.
- [117] G. N. Parsons, S. M. George, M. Knez, *MRS Bull.* **2011**, 36, 865.
- [118] C. Wang, D. Zhao, C. R. Grice, W. Liao, Y. Yu, A. Cimaroli, N. Shrestha, P. J. Roland, J. Chen, Z. Yu, P. Liu, N. Cheng, R. J. Ellingson, X. Zhao, Y. Yan, *J. Mater. Chem. A* **2016**, 4, 12080.
- [119] Z. Chen, G. Yang, X. Zheng, H. Lei, C. Chen, J. Ma, H. Wang, G. Fang, *J. Power Sources* **2017**, 351, 123.
- [120] M. M. Tavakoli, F. Giordano, S. M. Zakeeruddin, M. Gratzel, *Nano Lett.* **2018**, 18, 2428.
- [121] Y. Lee, S. Paek, K. T. Cho, E. Oveisi, P. Gao, S. Lee, J.-S. Park, Y. Zhang, R. Humphry-Baker, A. M. Asiri, M. K. Nazeeruddin, *J. Mater. Chem. A* **2017**, 5, 12729.
- [122] K.-H. Jung, J.-Y. Seo, S. Lee, H. Shin, N.-G. Park, *J. Mater. Chem. A* **2017**, 5, 24790.
- [123] Z. Zhu, Y. Bai, X. Liu, C. C. Chueh, S. Yang, A. K. Jen, *Adv. Mater.* **2016**, 28, 6478.
- [124] Q. Dong, Y. Shi, K. Wang, Y. Li, S. Wang, H. Zhang, Y. Xing, Y. Du, X. Bai, T. Ma, *J. Phys. Chem. C* **2015**, 119, 10212.
- [125] Z. Zhu, X. Zheng, Y. Bai, T. Zhang, Z. Wang, S. Xiao, S. Yang, *Phys. Chem. Chem. Phys.* **2015**, 17, 18265.
- [126] Q. Liu, M.-C. Qin, W.-J. Ke, X.-L. Zheng, Z. Chen, P.-L. Qin, L.-B. Xiong, H.-W. Lei, J.-W. Wan, J. Wen, G. Yang, J.-J. Ma, Z.-Y. Zhang, G.-J. Fang, *Adv. Funct. Mater.* **2016**, 26, 6069.
- [127] S. Li, P. Zhang, H. Chen, Y. Wang, D. Liu, J. Wu, H. Sarvari, Z. D. Chen, *J. Power Sources* **2017**, 342, 990.
- [128] S. Li, P. Zhang, Y. Wang, H. Sarvari, D. Liu, J. Wu, Y. Yang, Z. Wang, Z. D. Chen, *Nano Res.* **2016**, 10, 1092.
- [129] G. Lu, J. Xu, J. Sun, Y. Yu, Y. Zhang, F. Liu, *Sens. Actuator B Chem.* **2012**, 162, 82.
- [130] P. Wang, J. Zhao, J. Liu, L. Wei, Z. Liu, L. Guan, G. Cao, *J. Power Sources* **2017**, 339, 51.
- [131] Z. Xiao, C. Bi, Y. Shao, Q. Dong, Q. Wang, Y. Yuan, C. Wang, Y. Gao, J. Huang, *Energy Environ. Sci.* **2014**, 7, 2619.
- [132] J. You, Z. Hong, Y. M. Yang, Q. Chen, M. Cai, T. B. Song, C. C. Chen, S. Lu, Y. Liu, H. Zhou, Y. Yang, *ACS Nano* **2014**, 8, 1674.
- [133] C. Roldán-Carmona, O. Malinkiewicz, A. Soriano, G. Mínguez Espallargas, A. García, P. Reinecke, T. Kroyer, M. I. Dar, M. K. Nazeeruddin, H. J. Bolink, *Energy Environ. Sci.* **2014**, 7, 994.
- [134] W. Chen, Y. Wu, Y. Yue, J. Liu, W. Zhang, X. Yang, H. Chen, E. Bi, I. Ashraful, M. Grätzel, L. Han, *Science* **2015**, 350, 944.
- [135] Y. Wu, X. Yang, W. Chen, Y. Yue, M. Cai, F. Xie, E. Bi, A. Islam, L. Han, *Nat. Energy* **2016**, 1, 16148.
- [136] K. O. Brinkmann, J. Zhao, N. Pourdavoud, T. Becker, T. Hu, S. Olthof, K. Meerholz, L. Hoffmann, T. Gahlmann, R. Heiderhoff, M. F. Oszajca, N. A. Luechinger, D. Rogalla, Y. Chen, B. Cheng, T. Riedl, *Nat. Commun.* **2017**, 8, 13938.
- [137] E. Bi, H. Chen, F. Xie, Y. Wu, W. Chen, Y. Su, A. Islam, M. Grätzel, X. Yang, L. Han, *Nat. Commun.* **2017**, 8, 15330.
- [138] M. Jung, Y. C. Kim, N. J. Jeon, W. S. Yang, J. Seo, J. H. Noh, S. I. Seok, *ChemSusChem* **2016**, 9, 2592.
- [139] S. Ye, W. Sun, Y. Li, W. Yan, H. Peng, Z. Bian, Z. Liu, C. Huang, *Nano Lett.* **2015**, 15, 3723.
- [140] Y. Dkhissi, S. Meyer, D. Chen, H. C. Weerasinghe, L. Spiccia, Y. B. Cheng, R. A. Caruso, *ChemSusChem* **2016**, 9, 687.

- [141] K. Wang, Y. Shi, L. Gao, R. Chi, K. Shi, B. Guo, L. Zhao, T. Ma, *Nano Energy* **2017**, *31*, 424.
- [142] Z. Liu, P. You, C. Xie, G. Tang, F. Yan, *Nano Energy* **2016**, *28*, 151.
- [143] I. Jeon, T. Chiba, C. Delacou, Y. L. Guo, A. Kaskela, O. Reynaud, E. I. Kauppinen, S. Maruyama, Y. Matsuo, *Nano Lett.* **2015**, *15*, 6665.
- [144] J. Ha, H. Kim, H. Lee, K.-G. Lim, T.-W. Lee, S. Yoo, *Sol. Energy Mater. Sol. Cells* **2017**, *161*, 338.
- [145] P. Docampo, J. M. Ball, M. Darwich, G. E. Eperon, H. J. Snaith, *Nat. Commun.* **2013**, *4*, 2761.
- [146] C. Wang, D. Zhao, Y. Yu, N. Shrestha, C. R. Grice, W. Liao, A. J. Cimaroli, J. Chen, R. J. Ellingson, X. Zhao, Y. Yan, *Nano Energy* **2017**, *35*, 223.
- [147] C. Wang, C. Xiao, Y. Yu, D. Zhao, R. A. Awni, C. R. Grice, K. Ghimire, I. Constantinou, W. Liao, A. J. Cimaroli, P. Liu, J. Chen, N. J. Podraza, C.-S. Jiang, M. M. Al-Jassim, X. Zhao, Y. Yan, *Adv. Energy Mater.* **2017**, *7*, 1700414.
- [148] C. Wang, L. Guan, D. Zhao, Y. Yu, C. R. Grice, Z. Song, R. A. Awni, J. Chen, J. Wang, X. Zhao, Y. Yan, *ACS Energy Lett.* **2017**, *2*, 2118.
- [149] Q. Dong, Y. Shi, C. Zhang, Y. Wu, L. Wang, *Nano Energy* **2017**, *40*, 336.
- [150] M. M. Tavakoli, K. H. Tsui, Q. Zhang, J. He, Y. Yao, D. Li, Z. Fan, *ACS Nano* **2015**, *9*, 10287.
- [151] B. Dou, E. M. Miller, J. A. Christians, E. M. Sanehira, T. R. Klein, F. S. Barnes, S. E. Shaheen, S. M. Garner, S. Ghosh, A. Mallick, D. Basak, M. van Hest, *J. Phys. Chem. Lett.* **2017**, *8*, 4960.
- [152] J. Xie, K. Huang, X. Yu, Z. Yang, K. Xiao, Y. Qiang, X. Zhu, L. Xu, P. Wang, C. Cui, D. Yang, *ACS Nano* **2017**, *11*, 9176.
- [153] L. Xiong, M. Qin, G. Yang, Y. Guo, H. Lei, Q. Liu, W. Ke, H. Tao, P. Qin, S. Li, H. Yu, G. Fang, *J. Mater. Chem. A* **2016**, *4*, 8374.
- [154] G. Yang, H. Lei, H. Tao, X. Zheng, J. Ma, Q. Liu, W. Ke, Z. Chen, L. Xiong, P. Qin, Z. Chen, M. Qin, X. Lu, Y. Yan, G. Fang, *Small* **2017**, *13*, 1601769.
- [155] K. G. Godinho, A. Walsh, G. W. Watson, *J. Phys. Chem. C* **2008**, *113*, 439.
- [156] Y. Bai, Y. Fang, Y. Deng, Q. Wang, J. Zhao, X. Zheng, Y. Zhang, J. Huang, *ChemSusChem* **2016**, *9*, 2686.
- [157] W. Ke, D. Zhao, C. Xiao, C. Wang, A. J. Cimaroli, C. R. Grice, M. Yang, Z. Li, C.-S. Jiang, M. Al-Jassim, K. Zhu, M. G. Kanatzidis, G. Fang, Y. Yan, *J. Mater. Chem. A* **2016**, *4*, 14276.
- [158] L. Kegelmann, C. M. Wolff, C. Awino, F. Lang, E. L. Unger, L. Korte, T. Dittrich, D. Neher, B. Rech, S. Albrecht, *ACS Appl. Mater. Interfaces* **2017**, *9*, 17245.
- [159] G. Yang, C. Wang, H. Lei, X. Zheng, P. Qin, L. Xiong, X. Zhao, Y. Yan, G. Fang, *J. Mater. Chem. A* **2017**, *5*, 1658.
- [160] L. Zuo, Q. Chen, N. De Marco, Y. T. Hsieh, H. Chen, P. Sun, S. Y. Chang, H. Zhao, S. Dong, Y. Yang, *Nano Lett.* **2017**, *17*, 269.
- [161] H.-S. Rao, B.-X. Chen, W.-G. Li, Y.-F. Xu, H.-Y. Chen, D.-B. Kuang, C.-Y. Su, *Adv. Funct. Mater.* **2015**, *25*, 7200.
- [162] J. Ma, G. Yang, M. Qin, X. Zheng, H. Lei, C. Chen, Z. Chen, Y. Guo, H. Han, X. Zhao, G. Fang, *Adv. Sci.* **2017**, *4*, 1700031.
- [163] Z. Xiao, Y. Yuan, B. Yang, J. VanDerslice, J. Chen, O. Dyck, G. Duscher, J. Huang, *Adv. Mater.* **2014**, *26*, 3068.
- [164] M. Campoy-Quiles, T. Ferenczi, T. Agostinelli, P. G. Etchegoin, Y. Kim, T. D. Anthopoulos, P. N. Stavrinou, D. D. Bradley, J. Nelson, *Nat. Mater.* **2008**, *7*, 158.
- [165] Y. Hou, X. Chen, S. Yang, C. Li, H. Zhao, H. G. Yang, *Adv. Funct. Mater.* **2017**, *27*, 1700878.
- [166] X. Yao, J. Liang, T. Li, L. Fan, B. Shi, C. Wei, Y. Ding, Y. Li, Y. Zhao, X. Zhang, *Sci. Chin. Mater.* **2017**, *61*, 65.
- [167] R. Azmi, W. T. Hadmojo, S. Sinaga, C.-L. Lee, S. C. Yoon, I. H. Jung, S.-Y. Jang, *Adv. Energy Mater.* **2018**, *8*, 1701683.
- [168] W. Zhang, Z. Ren, Y. Guo, X. He, X. Li, *Electrochim. Acta* **2018**, *268*, 539.
- [169] J. Song, E. Zheng, X.-F. Wang, W. Tian, T. Miyasaka, *Sol. Energy Mater. Sol. Cells* **2016**, *144*, 623.
- [170] D. Yang, R. Yang, K. Wang, C. Wu, X. Zhu, J. Feng, X. Ren, G. Fang, S. Priya, S. Liu, *Nat. Commun.* **2018**, *9*, 3239.
- [171] Y. Deng, E. Peng, Y. Shao, Z. Xiao, Q. Dong, J. Huang, *Energy Environ. Sci.* **2015**, *8*, 1544.
- [172] F. Ye, H. Chen, F. Xie, W. Tang, M. Yin, J. He, E. Bi, Y. Wang, X. Yang, L. Han, *Energy Environ. Sci.* **2016**, *9*, 2295.
- [173] M. Yang, Z. Li, M. O. Reese, O. G. Reid, D. H. Kim, S. Siol, T. R. Klein, Y. Yan, J. J. Berry, M. F. A. M. van Hest, K. Zhu, *Nat. Energy* **2017**, *2*, 17038.